DESIGN OF A DSP-BASED IMPEDANCE MEASURING INSTRUMENT FOR MULTIPHASE FLOWMETER

XIANG FANG

Design of a DSP-Based Impedance Measuring Instrument for Multiphase Flowmeter

by

©Xiang Fang

B.Eng., Nanjing University of Science and Technology, China (1996)

A thesis submitted to the
School of Graduate Studies
in partial fulfillment of the
requirements for the degree of
Master of Engineering

Faculty of Engineering and Applied Science
Memorial University of Newfoundland

May 2006

St. John's Newfoundland

Your file Votre référence
ISBN: 978-0-494-19358-7
Our file Notre référence
ISBN: 978-0-494-19358-7

Design of a DSP-Based Impedance Measuring Instrument for Multiphase Flowmeter

by

Xiang Fang

Abstract

Crude oil is a mixture of gas, oil and water. Knowing the ratio of these three components can help to optimize the production process. Multiphase flowmeters have therefore been designed and constructed in recent years. However, the costs of current multiphase flowmeters based on radiation techniques are too expensive. In order to overcome this drawback, a low-cost electrical impedance-based multiphase flowmeter is investigated in the research.

After numerical simulations and experiments, this thesis develops a DSP-based impedance measuring instrument that can obtain the impedance data from crude oil in real time. Experimental data show that the performance of this DSP-based impedance measuring instrument has good resolution and good linearity.

The work completed to date acts as a starting point from which improvements and extensions can be easily made and incorporated. In this regard, suggestions for future work are also presented.

Acknowledgements

I will begin by thanking my supervisor, Dr. Vlastimil Masek, who suggested this as my research topic, provided me complete freedom to try ideas and be essentially self-directed, and gave support when it was needed. Acknowledgement must also be given to Dr. Cecilia Moloney for the advice in the digital signal processing.

Many thanks to technicians Roy Crocker and Brian Power for helping me with the fabrications of the printed circuit boards and the experimental devices. I also wish to show my appreciation to my colleagues and friends, Andrew Oldford, Boluo Xie, Bradley Whittle, Eranda Harinath, Mark O'Rielly, and Weimin Huang for the discussions and suggestions at various stages of the work.

I also wish to thank the Faculty of Engineering and Applied Science, Memorial University of Newfoundland, for providing much needed laboratory space, equipment, and technical services to take this project from idea to implementation.

This work would not have been completed without the support from my parents and my wife who were always there to accentuate the positive side of graduate studies.

Financial support from the Atlantic Innovation Fund and from the Natural Sciences and Engineering Research Council (NSERC) of Canada is greatly acknowledged.

Contents

List of Figures

List of Tables

Chapter 1

Introduction

The impedance is an important parameter in electrical measurements. Normally, different materials show different impedance quantities in the measurement [1]. Measurement of an electrical impedance is used in many sensing applications ranging from process industries to the civil sector. In this thesis, the electrical impedance measurement is employed to measure the composition of crude oil that is essential to the oil production optimization [2].

Many detection techniques can be used in impedance measurement, such as resonance, oscillation, charge transfer and AC bridge [3]. For precise measurement, AC bridge is chosen as the signal input circuit for this research project. On the other hand, in the signal demodulation, a digital signal processing (DSP) technique is used to improve the measuring accuracy and stability, which is the most important part of this thesis.

1.1 Principle of the Impedance Measurement

1.1.1 Definitions in the impedance measurement

This section will begin by presenting several fundamental concepts used in this thesis.

Definition 1 Capacitance [4]: *In a capacitor or system of conductors and dielectrics, the property that permits the storage of electrically separated charges when potential differences exist between the conductors. Capacitance is related to charge and voltage as follows: $C = Q/V$, where C is the capacitance in farads, Q is the charge in coulombs, and V is the voltage in volts.*

Definition 2 Permittivity [4]: *The permittivity (previously the term dielectric constant was used) of a dielectric medium is a measure of its ability to be electrically polarized when exposed to an electric field. The capacitance of an electrical capacitor is proportional to the permittivity of the dielectric medium. In practice, when the term permittivity is used, it is usually referred to as the relative permittivity.*

Definition 3 Conductance [5]: *The conductance is the ratio of a current in the conductor to the potential difference between its ends. Reciprocal of resistance. The standard unit of conductance is siemens.*

Definition 4 Conductivity [4]: *The ability of a material to conduct electrical current. In isotropic material the reciprocal of resistivity. Unit is siemens/m.*

Definition 5 Capacitive Sensors [6]: *Capacitive sensors electronically measure the capacitance between two or more conductors in a dielectric environment, usually air or a liquid.*

Capacitive sensors can be constructed as large electrodes or integrated into a microchip. They are normally used for non-contact sensing, such as position encoding, liquid level sensing, proximity detection and flow measurement [6]. In this project,

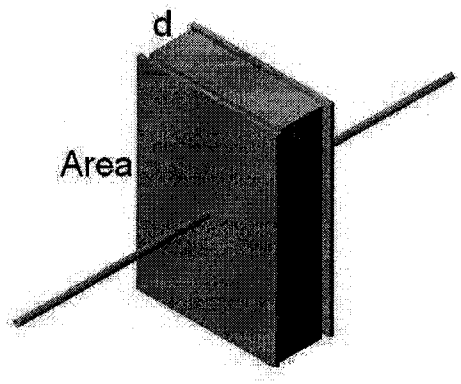

Figure 1-1: Parallel plate capacitor diagram.

the capacitance sensor is employed to measure the material properties between two sensor electrodes. It should be noted that the impedance measurement discussed in this thesis refers to the capacitance measurement and the conductance measurement.

1.1.2 The capacitance of parallel plates

In Figure (1-1), the capacitance [6] of a parallel plate capacitor can be calculated by

$$C = \frac{\varepsilon_0 \varepsilon_r A}{d} \tag{1.1}$$

where

C=Capacitance, frads

ε_0=Free space permittivity, 8.854×10^{-12}, frads/meters

ε_r=Relative permittivity of the material between plates, 1 for vacuum

A=Plate area, square meters

d=Spacing, meters

When the area and spacing of parallel plates are constant, the capacitance will be dependent only on the relative dielectric constant of the material between two parallel plates. It is the reason why a capacitive sensor is employed to measure properties of crude oil in this thesis.

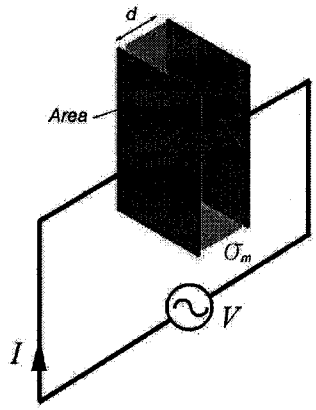

Figure 1-2: The diagram for obtaining the conductance from a capacitive sensor.

1.1.3 The conductance and conductivity

In Figure (1-2), the conductance [7] between two plates can be calculated by

$$G_m = \frac{1}{R_m} \tag{1.2}$$

where

G_m=Conductance of the material between two plates, siemens

R_m=Resistance of the material between two plates, ohm (Ω)

The resistance of the material between two plates can be obtained by Ohm's Law, namely, the resistance is equal to the quotient of the voltage applied on the capacitive sensor and the current flowing through the capacitive sensor ($R_m = V/I$).

Then, the conductivity [7] of this material can obtained by

$$\sigma_m = \frac{G_m \cdot d}{A} \tag{1.3}$$

where

G_m=Conductance of the material between two plates, siemens

A=Plate area, square meters

d=Spacing, meters

1.2 INCA and PPSC Project

1.2.1 The INCA center

INCA stands for the center for INstrumentation, Control and Automation. As a part of Memorial University of Newfoundland, INCA provides the resources for both research and education. INCA is involved in several major research projects such as the PPSC project and the RAVEN project.

1.2.2 PPSC Project

This research work is a part of the PPSC (PanAtlantic Petroleum Systems Consortium) project. The goal of this component of the project is to design an impedance-based multiphase flowmeter. The objectives of this research project are:

1. Design a novel impedance sensor which can form stratified flow and only cause a small pressure drop across the sensor.
2. Design an instrument which can measure capacitances and conductances from the multiphase flow of crude oil.
3. Build evaluating models from measuring results to obtain the component fractions of gas/oil/water in crude oil.
4. Determine the flow velocity and the mass flow rate in the pipe.
5. Design a multiphase flowmeter based on the above research results.

This thesis is concentrating on objective 2; however, comments to other objectives are also provided.

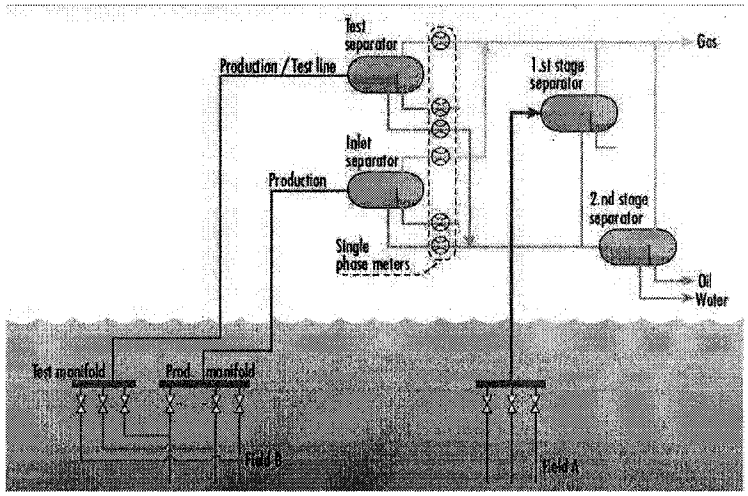

Figure 1-3: The diagram for offshore conventional component fraction measurements [8].

1.3 Industry Problems

Oil & Gas plays an important role in our modern society as an energy source as well as a raw material for many products. After exploitations over the last century, many oil reserviors on land will soon be exhausted. In order to deal with this severe challenge, oil producers start exploiting the subsea oil reserviors to sustain their requirements for crude oil.

The offshore oil production is very different from the oil production on land. Due to its nature, many land-based techniques must be redesigned to meet the new requirements. Figure (1-3) illustrates a conventional offshore component fraction measuring setup on the petroleum platform, where a test separator and several single-phase flowmeters are used in the measurements; however, this is costly solution and requires an extra space on the platform. In addition, this method can only obtain offline component fraction data, whereas the production optimization needs the real-time component fractions. Multiphase flowmeters in Figure (1-4) are considered to meet this requirement. In recent years, many different techniques have been applied in the design of a multiphase flowmeter, such as: Gamma-ray attenuation [8], microwave

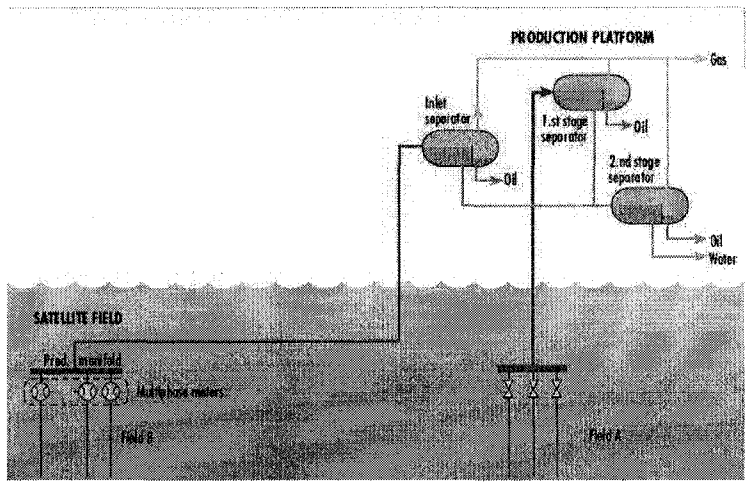

Figure 1-4: The diagram for individual well monitoring of multiphase meters [8].

attenuation, pulsed neutron activation (PNA), nuclear magnetic resonance (NMR) and electrical impedance techniques [9].

Although some of these multiphase flowmeters emerged on the market recently, few of them can be used in the offshore petroleum industry due to their measuring performance [10]. For instance, the flowmeters based on gamma-ray attenuation, microwave attenuation and electrical impedance techniques are flow regime dependent. The flowmeters based on PNA and NMR are inherently flow regime independent, but the technologies employed are too complicated and are extremely costly. If these five techniques are compared, the electrical impedance technique will show some advantages over others, such as: low cost, fast dynamic response, and no safety problems with nuclear radiation.

1.4 Research Objectives

As mentioned in the previous section, the impedance sensor is dependent on the flow regime. To overcome this problem, a mixer can be used to form a homogenous flow in the front of the impedance sensor, but it may generate a pressure drop thus needs more pumping power for the oil transportation. Moreover, the homogenous flow is not

good for the later separation process. To solve this problem, we assume to rotate the multiphase flow and then form a stratified flow due to the different specific gravities of the gas/oil/water components.

This thesis describes a design of an instrument which can measure the capacitance and the conductance of crude oil. In addition, the following topics will be addressed:

1. The method to detect small capacitances between two electrodes regardless of the stray capacitance among electrodes, cables and shields.

2. The method to separate the capacitance signal and the conductance signal from a common sensor output.

3. The performance comparison between an analog signal processing and a digital signal processing.

4. The way to maintain its accuracy over the lifetime of the instrument.

5. The way to perform a real-time data acquisition and analysis simultaneously.

6. The way to transmit the measuring results to the supervisory system or receive the setup commands from the supervisory system.

A stray-immune circuit is chosen to remove the stray capacitance for the impedance sensor, which is based on the "Visual Ground" principle of the operational amplifier. In an AC circuit, the currents flowing through a resistor and a capacitor will have a 90° phase difference. An in-phase and a quadrature phase-sensitive demodulator (PSD) are therefore employed to distinguish the capacitance component and conductance component from a same sensor output signal. However, the performance of the PSDs is mainly dependent on the reference signals. For example, a 90° phase shifted reference signal is needed in the quadrature demodulation for detecting the capacitance component, whereas generating a precise and stable 90° phase shifted analog signal is a challenging task for any designer.

In order to reach the required accuracy and stability of the measurement, a digital signal processing (DSP) solution is considered in the design. The digital solution is able to remove errors from the signal processing; however, attention must be paid to the errors in Analog-to-Digital Converter (ADC), which can significantly reduce the accuracy of the digital solution. A DSP microprocessor (TMS320F2812) is employed in this thesis, which operates at 150MHz (6.67ns Cycle Time), has 12-Bit ADC, supports up to 12.5MSPS sampling, and can perform data acquisition and DSP analysis simultaneously [11]. For external communication, this chip supports Serial Peripheral Interface (SPI), Serial Communications Interface (SCI) and Enhanced Controller Area Network (eCAN). For the implementation reason, a SCI is chosen as the communication interface between the DSP chip and the supervisory computer.

1.5 Organization of Thesis

Chapter 2 gives a discussion on the literature in several related areas. Chapter 3 illustrates the design and implementation of an impedance measuring instrument. Chapter 4 describes the implementation of the experiments and the analysis of the experimental results. Conclusions and suggestions for future work are presented in Chapter 5.

Chapter 2

Review of Related Work

A constantly increasing consumption of the oil over last years drives the industry to search for new deposits at sea. However, offshore oil & gas industry presents many challenges in comparison to the land-based production, such as: harsh marine environment, the separation process on the moving platform, and large pressures in the pipeline that links from producing wells to the surface production platform.

In general, each well is producing a different amount of oil, gas and produced water, so managing a production field of few tens of wells is not an easy task. As a result, providing a knowledge about the produced composition, the ratio of gas/oil/water, can greatly enhance the process optimization. Conventionally, a test separator is employed in the measurement; however, this method only offers the off-line ratio of each component and needs a large space on the surface of the production platform. Therefore, in order to obtain real-time information from each well and save the space on the production platform, a subsea well-head mounted multiphase flowmeter is needed in the offshore industry.

2.1 Multiphase Flow

One of the reasons for halting the success of the development of multiphase flowmeters comes from the crude oil flow, known as multiphase flow. It is common in the oil & gas industry, and it is difficult to measure, predict and model. Normally, the flow structures are affected by the proportions, physical properties and velocity of every component inside crude oil [10]. By observing the flow patterns in the transparent pipe, the researchers summarized them into several flow regimes. The distribution of the different components in crude oil varies with flow regimes and is usually not under the production control [4]. Process conditions and the orientation and geometry of the pipe can change flow regimes from one to another smoothly and continuously [10]. Determining flow regime is therefore becoming a hard task to any designer in the multiphase flow metering.

Figures (2-1) and (2-2) list common flow regimes in the pipe. It should be noted that the superficial gas velocity in these figures is the gas velocity when the gas is flowing in the pipe without liquids; similarly, the superficial liquid velocity is defined [4].

Vertical flows

With increasing the superficial gas velocity, the multiphase flow will change flow regimes from bubble to slug, then to churn and finally to annular. Note that the multiphase flow in Figure (2-1) will remain in annular flow for all superficial liquid velocities when the superficial gas velocity is greater than a certain speed.

Horizontal flows

The transitions are also functions of superficial gas and liquid velocities. It is also noted that the data listed in Figure (2-2) is only valid for a specific pipe, a certain pressure and a specific multiphase flow.

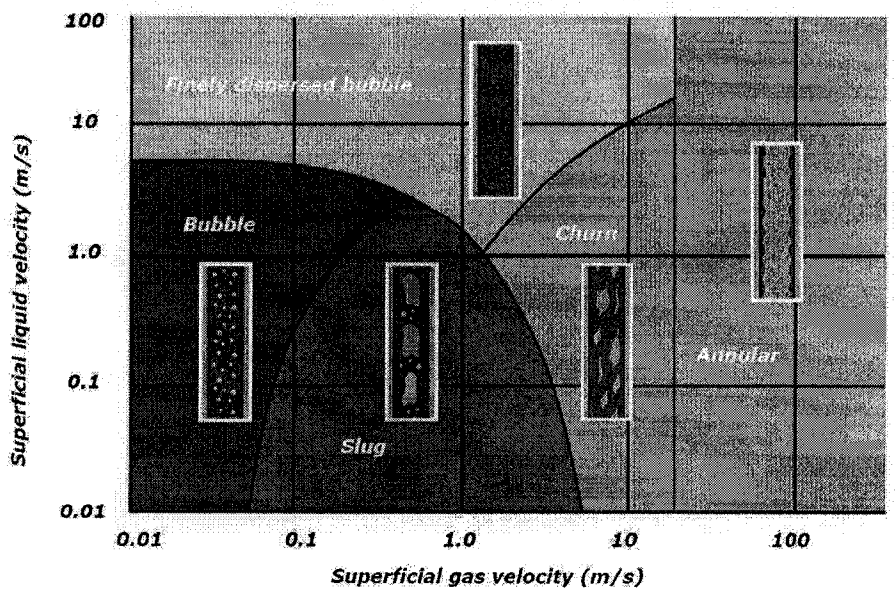

Figure 2-1: A generic two-phase vertical flow map, note that superficial velocities are used along the axis [4].

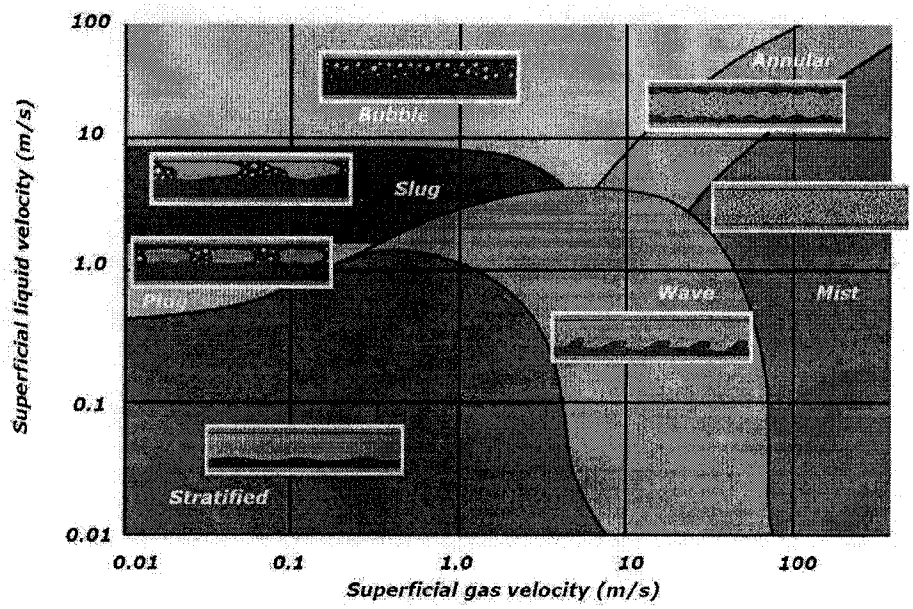

Figure 2-2: A generic two-phase horizontal flow map, note that superficial velocities are used along the axis [4].

2.2 Current Multiphase Flowmeter Technology

Currently, many types of multiphase flowmeters are available in the market. In general, they use a combination of two or more of the following measurement techniques [4]:

- Electromagnetic measurement principles
  - Microwave
  - Capacitance
  - Conductance
- Gamma-ray densitometry or spectroscopy
- Neutron interrogation
- Differential pressure using Venturi, V-cone or other restriction
- Positive displacement
- Ultrasonic
- Cross-correlation of electromagnetic, radioactive, ultrasound signals (to calculate flow velocities)

Detailed information about four commercial multiphase flowmeters is presented below.

2.2.1 Agar MPFM-400 SERIES Multiphase Flowmeter

The Agar MPFM-400 Series Meters are designed to handle a wide range of flow rates. The Agar MPFM-400 Series extends the dynamic range of the gas and void fraction capacity of the Agar MPFM-300 Series multiphase flowmeters by adding a Fluidic Flow Diverter (FFD®) Device and gas bypass loop. The FFD® Device uses the

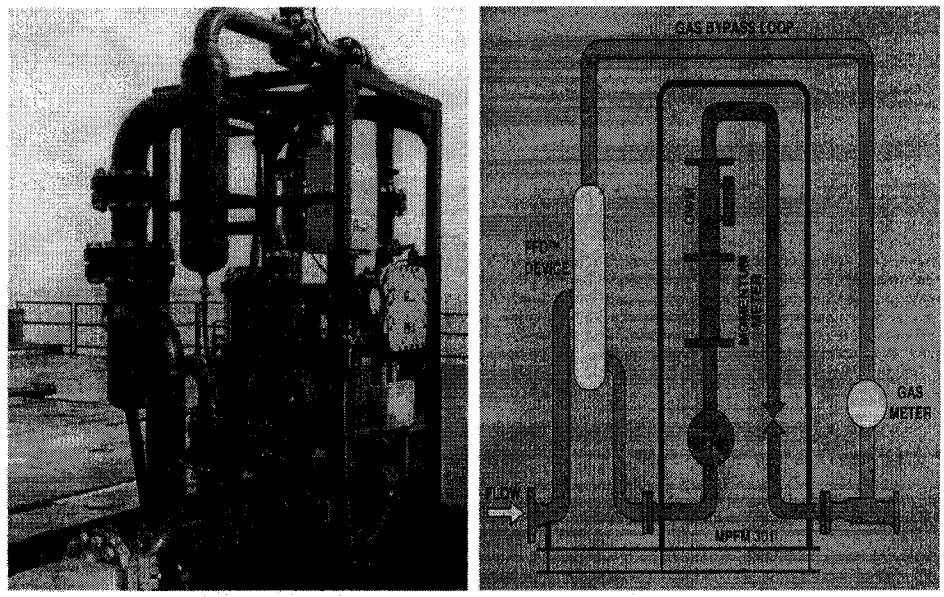

(a) Installed on an Offshore Platform. (b) Schematic Diagram.

Figure 2-3: The diagrams for Agar MPFM-400 [12].

difference in flow momentum of the gas and the liquid to separate them into two different loops. Most of the free gas in the stream flows into a gas bypass loop around the core MPFM-300. The remaining fluids flow through the core MPFM-300 Series system [12].

The design of this multiphase flowmeter is based on the partial separation method. Namely, multiphase flow is first separated into a gas dominant flow and a liquid dominant flow, and then two relatively simple measurements are performed on each loop. Testing results showed that this multiphase flowmeter was suitable for high gas fraction flows with an accuracy of $\pm$ 10% [9].

2.2.2 Framo Multiphase Flowmeter

Framo multiphase flowmeter is independent of flow regimes by using a mixer to homogenize flows before the measurement. The schematic diagram of this multiphase flowmeter is shown in Figure (2-4). In the measurement part, Venturi and dual energy

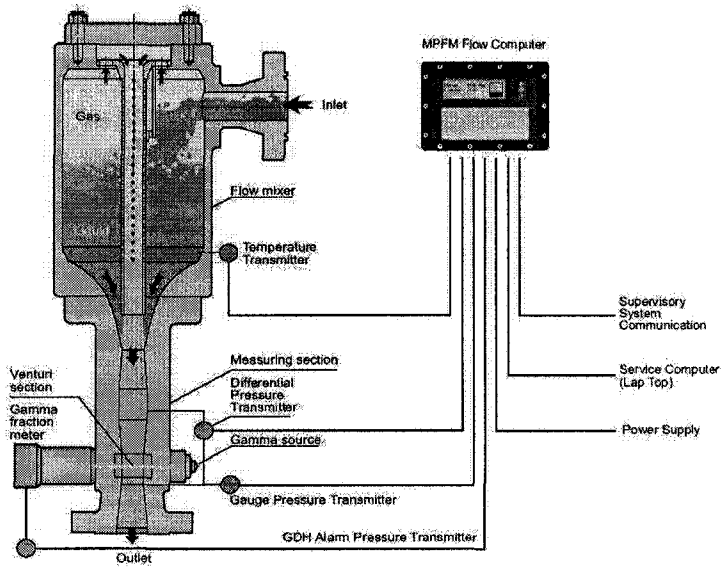

Figure 2-4: The schematic diagram for Framo multiphase flowmeter[13].

gamma-ray are employed to obtain the flow rate and the component fractions of each phase respectively [8]. Testing results have shown that it has an accuracy of $\pm$ 5%. Also, this multiphase flowmeter supports both topside and subsea installation; it is therefore used in many offshore projects. However, the expense of this multiphase flowmeter is a substantial barrier for applying it widely to offshore applications [9].

2.2.3 Roxar MPFM 1900VI Multiphase Flowmeter

Compared with two multiphase flowmeters discussed in the previous subsections, Roxar MPFM 1900VI® multiphase flowmeter does not need any extra devices, such as a mixer or separator installed before measurements; however, more measuring techniques are involved for this flow regime independent multiphase flowmeter. Not only Venturi and gamma-ray measurements are employed in the design, but also impedance measurements are introduced for this purpose [14]. Similar to Framo multiphase flowmeter, this kind of flowmeter has both good accuracy and a high cost. However, this high cost limits it to be used in most offshore projects.

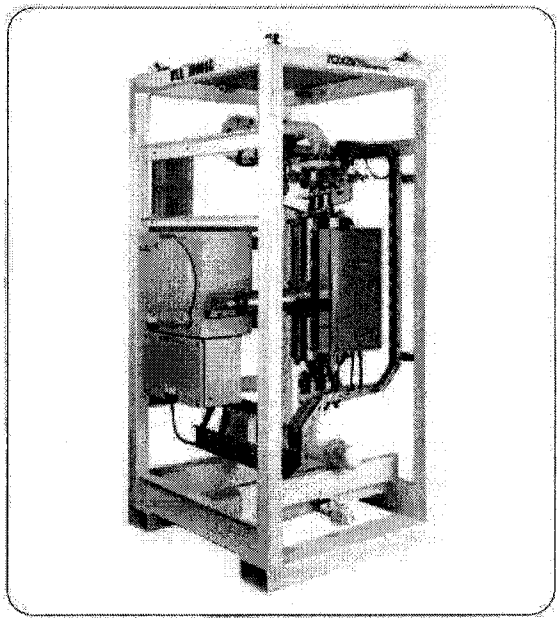

Figure 2-5: Roxar MPFM 1900VI multiphase flowmeter[14].

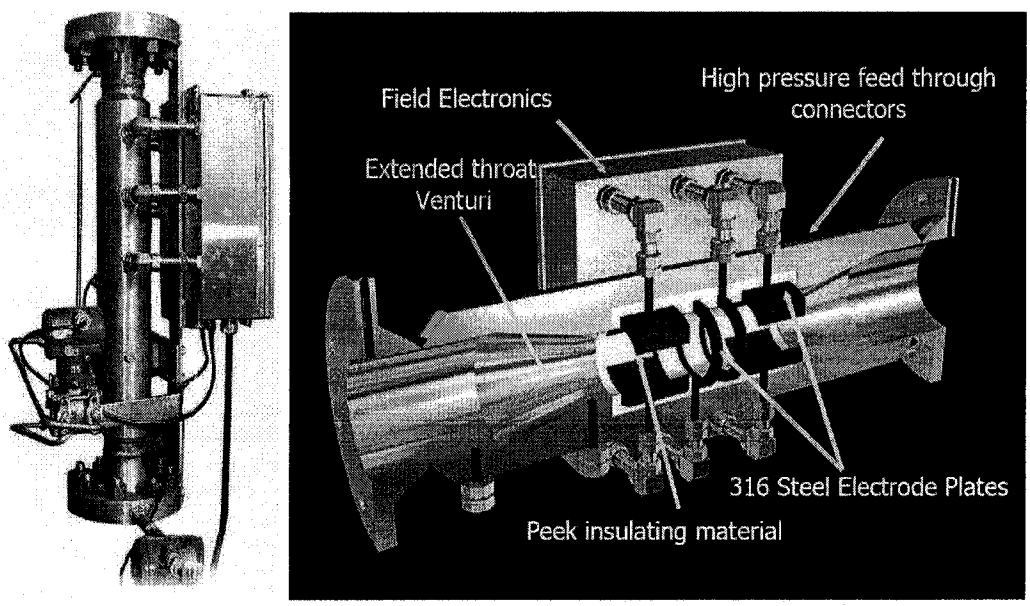

(a) Front View.

(b) Cutaway View.

Figure 2-6: Flowsys multiphase flowmeter[7].

2.2.4 Flowsys Multiphase Flowmeter

Unlike three multiphase flowmeters discussed above, Flowsys^{TM} multiphase flowmeter in Figure (2-6) is a relatively low-cost multiphase flowmeter. It employs an electrical impedance technique instead of radiation techniques. However, it is only used in land-based applications.

2.2.5 Research Work in PPSC Project

As mentioned in Chapter 1, the offshore industry needs a low-cost multiphase flowmeter that can be installed on every well head to monitor the crude oil composition in real time. Compared with above four multiphase flowmeters, the impedance-based multiphase flowmeter is considered due to its low cost characteristics.

Since the impedance-based multiphase flowmeter is dependent on flow regimes, its accuracy is currently not sufficient for real-time production monitoring. A new design will be carried out in the future. For example, a cyclone flow rotator can be added to convert an arbitrary flow into a stratified flow before the measurement takes place. In this way, the performance of the impedance-based multiphase flowmeter can be significantly improved.

In order to meet the requirement of the subsea well-head installation, we assume to only install the measuring electrodes in subsea, whereas the field electronics are installed on the topside of the production platform. As shown in Figure (2-7), long shield cables can be used between the electrodes and the field electronics. However, this new configuration generates large stray capacitances between cables and shields. Therefore, the research work in this thesis focuses on the impedance signal detection and demodulation under the presence of large stray capacitances.

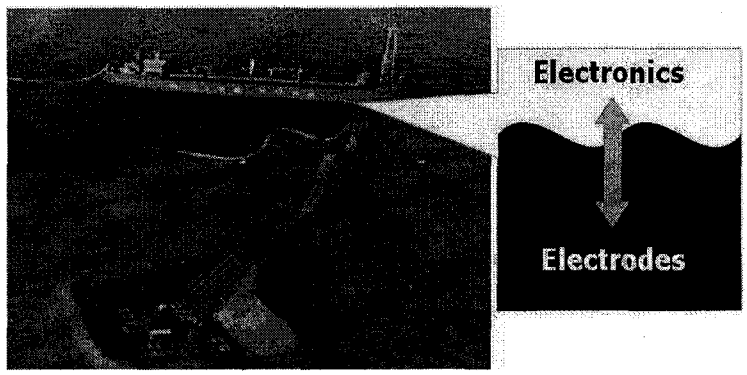

Figure 2-7: The diagram for offshore oil production [15].

2.3 Detections and Demodulations of Impedance Signals

Figure (2-8a) shows an impedance sensor which is built by two parallel plates and a shielding screen. Also, a sensor schematic circuit is drawn in Figure (2-8b). In this project, the stray capacitances C_{s_1}, C_{s_2} (between electrodes and the shielding screen) and the parasitic capacitances C_{p_1}, C_{p_2} (between cables and the shielding screen) are several orders larger than the measured capacitance C_x. As a result, the impedance measuring circuit should be designed to remove these stray capacitances.

In addition, for simplicity in this thesis, C_{s_1} will stand for the total capacitances of C_{s_1} and C_{p_1}, and C_{s_2} will denote the total capacitances of C_{s_2} and C_{p_2}.

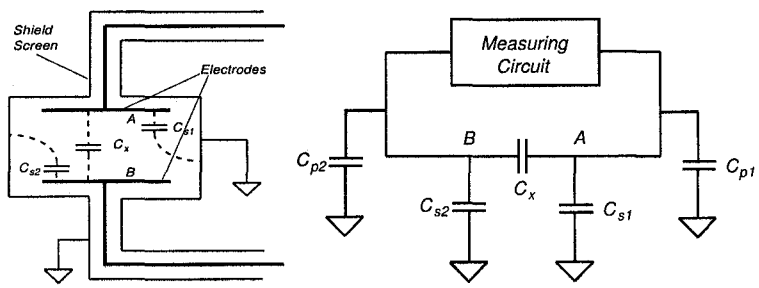

(a) Sensor structure. (b) Equivalent circuit.

Figure 2-8: The diagrams for an impedance sensor [3].

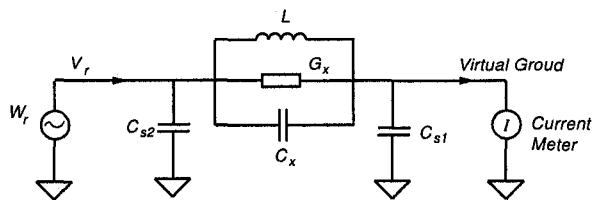

Figure 2-9: The measuring circuit based on the resonance method [3].

In general, the measuring circuit can be arranged into four main categories: resonance, oscillation, charge/discharge and AC bridge methods [3].

2.3.1 The resonance method

In Figure (2-9), C_{s_1} and C_{s_2} are shunted by the power source and the current detector respectively. Thus, they have no effect to the parallel LCG circuit. The steady-state admittance of the LCG circuit is [16]:

$$Y = G_x + j(\omega C_x - \frac{1}{\omega L}) \tag{2.1}$$

This circuit is tuned to resonance when the voltage applied to this circuit and the current flowing this circuit are in phase. It is corresponding to a purely real admittance [16], namely, $\omega C_x - 1/\omega L = 0$.

Thus, the capacitance C_x can be derived by

$$C_x = \frac{1}{\omega^2 L} \tag{2.2}$$

Moreover, the conductance G_x can be obtained by

$$G_x = \frac{I_r}{V_r} \tag{2.3}$$

Measurements based on this method require several operating steps such as adjusting the resonance frequency, detecting the resonance condition and calculating

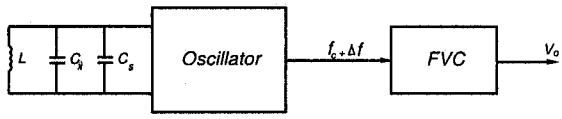

Figure 2-10: The measuring circuit based on the LC oscillator method [3].

the sensing capacitance and conductance [3]. The first two steps are often controlled manually; therefore, this method is not suitable for the real-time impedance measurement.

2.3.2 The LC oscillation method

Figure (2-10) shows a schematic diagram for a typical LC oscillation measurement. In general, this method is used to measure the change in the measured capacitance, which can be expressed as [3]:

$$\Delta C_x = \frac{2(C_x + C_s)}{f_0} \Delta f \tag{2.4}$$

where

C_s=the overall stray capacitance

C_x=The capacitance between two electrodes

f_0=The standing oscillation frequency

As shown in Figure (2-10), a Frequency-to-Voltage Converter (FVC) is employed to detect the change in the oscillation frequency (Δf), and then the change in the measured capacitance (ΔC_x) can be calculated by Equation (2.4). However, the stray capacitance (C_s) is included in the measurement, and this method cannot measure the conductance component from the sensor. Therefore, this method is also not suitable for the impedance measurements in this thesis.

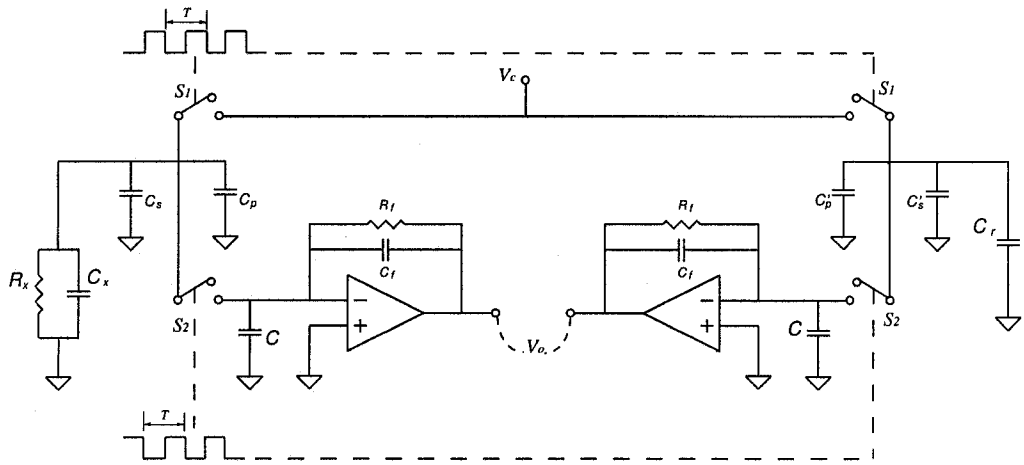

Figure 2-11: The measuring circuit based on the charge/discharge method [3].

2.3.3 The charge/discharge method

Figure (2-11) draws a schematic diagram for the charge/discharge method [3]. The charge and discharge operations are controlled by two pairs of switches (S_1, S_2). When S_1 switches are on and S_2 switches are off, the sensor and the reference capacitor are charged. On the contrary, they release the charge to detector circuits when S_1 switches are off and S_2 switches are on. If C and R_fC_f in the charge detector are selected to large values, the outputs [3] of the detectors will be denoted by

$$V_x = fV_cR_f(C_x + C_s + C_p) \tag{2.5}$$

$$V_r = fV_cR_f(C_r + C'_s + C'_p) \tag{2.6}$$

where

f=The switching frequency of the S_1 and S_2

V_c=The charging voltage

R_f=The resistance of the feedback resistors

As shown in Figure (2-11), the final voltage output (V_o) is the difference of two

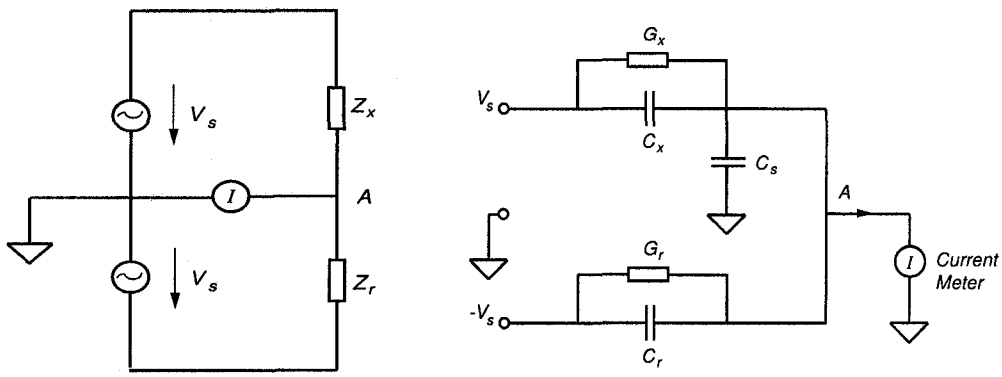

(a) AC bridge. (b) Equivalent circuit.

Figure 2-12: The diagrams for AC bridge method [3].

detector outputs (V_x and V_r) [3], namely,

$$V_o = fV_cR_f[(C_x - C_r) + (C_s - C_s') + (C_p - C_p')] \tag{2.7}$$

As the previous LC oscillator circuit, this circuit is not a stray-immune circuit. Therefore, it is not suitable for the research in this thesis.

2.3.4 The AC bridge method

The AC bridge method has a long history since Sir Charles Wheatstone employed it to the comparison of resistance in 1843 [17]. Nowadays, it is considered as the most accurate and stable method for impedance measurements. A basic AC bridge circuit is shown in Figure (2-12a). If no current is detected by the current detector, this bridge will be balanced. The measured impedance can be obtained by

$$Z_x = Z_r \tag{2.8}$$

In most cases, this bridge is not balanced. According to the equivalent circuit in Figure (2-12b), the unbalanced current flowing through the current detector can be

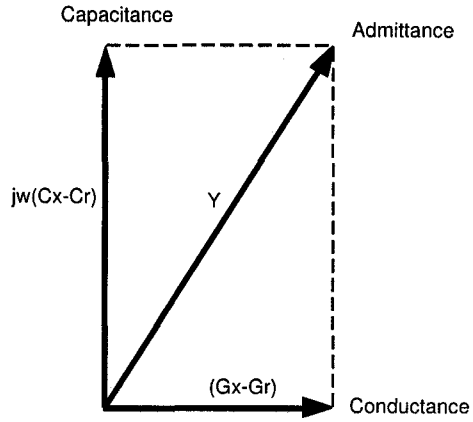

Figure 2-13: The phase diagram for conductance and capacitance components.

denoted as:

$$I = V_s[(G_x - G_r) + j\omega(C_x - C_r)] \tag{2.9}$$

In this equation, the bridge output current is composed of two 90° phase difference signals, which are shown in Figure (2-13). Then, both an in-phase and a quadrature phase-sensitive demodulator are used to separate the conductance component and the capacitance component from this current signal respectively. Similar to the resonance method, this method is also based on the stray-immune design. Therefore, the AC bridge circuit is chosen for signal detection in this thesis.

2.3.5 The impedance reference

The main purpose for using impedance references (C_r and G_r) in the circuit in Figure (2-12b) is to reduce the drifts caused by the power source and temperature. However, if the references are not stable in the measurement, the measuring accuracy will be worse than the accuracy of a directly measuring circuit. A thermal coupling method is therefore proposed to construct the impedance references and improve their stabilities in the multiphase flow measurements. In Figure (2-14), a thermal coupling device is used to balance the temperature between the measured flow and the reference flow.

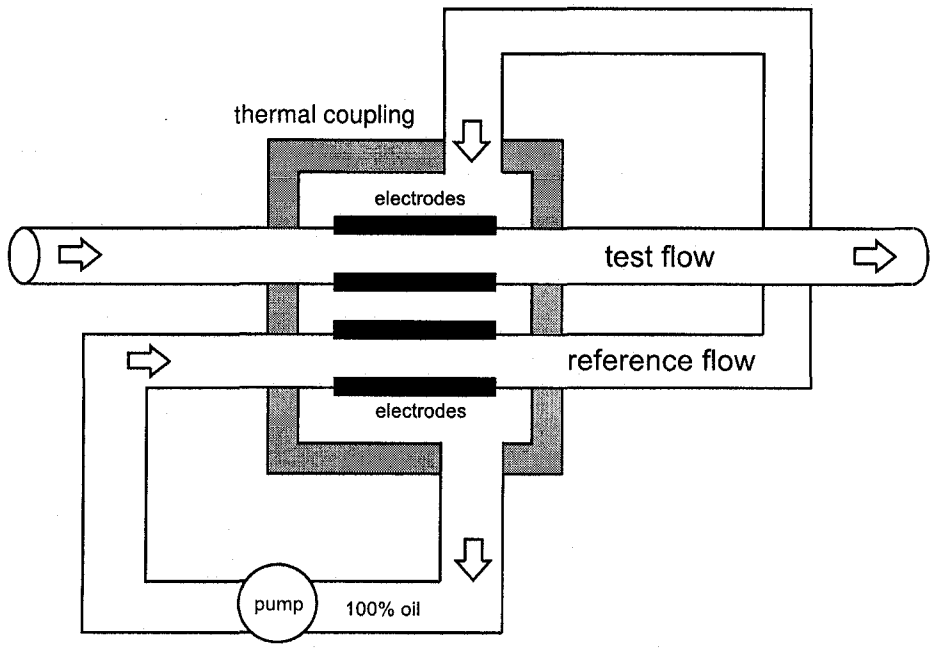

Figure 2-14: A thermal coupling reference schematic diagram [6].

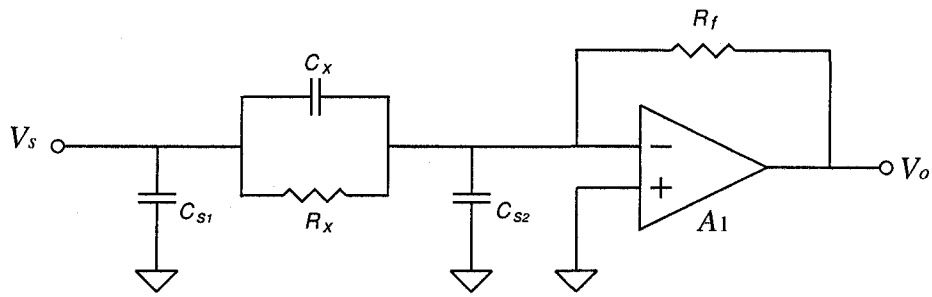

Figure 2-15: A simplified measuring circuit schematic diagram.

2.3.6 Simplified circuit and current detector

As discussed in the previous subsection, constructing a stable reference system is a complex task. Moreover, the research emphasis of this thesis is on the signal detection and demodulation, so the measuring circuit described in this thesis will not include the impedance reference part. Namely, the current detector will only measure the current flowing through the sensor. A simplified schematic diagram of the measuring circuit [18] is illustrated in Figure (2-15). In this diagram, the stray capacitance C_{s_1} is shunted by the power source, so it has no effect on the sensor output current I_s. In addition, C_{s_2} is connected to the virtual ground of the operational amplifier ($A1$), so no current flows into C_{s_2}. In other words, this stray capacitance is canceled in the measuring circuit. Therefore, this simplified measuring circuit is also a stray-immune circuit. Consequently, the current flowing through the sensor can be expressed as

$$I_s = V_s(G_x + j\omega C_x) \tag{2.10}$$

At the end of this stage, the sensor current (I_s) is transferred to a voltage signal (V_o) by a current detector ($A1$). Later, an in-phase and a quadrature phase-sensitive demodulator (PSD) will be employed to distinguish conductance component and capacitance component from this voltage signal (V_o).

2.3.7 Signal Demodulation

As can be seen in Figure (2-16), phase-sensitive demodulators (PSDs) play a pivotal role in this stage. In terms of the AC circuit theory, the currents flowing through a resistor and a capacitor will have a 90° phase difference. Two PSDs are therefore used to demodulate the in-phase component and the quadrature component from the current detector output (V_o). Finally, the sensor measured conductance can be obtained from the in-phase PSD output ($V_{dc,RES}$), and the sensor measured capacitance

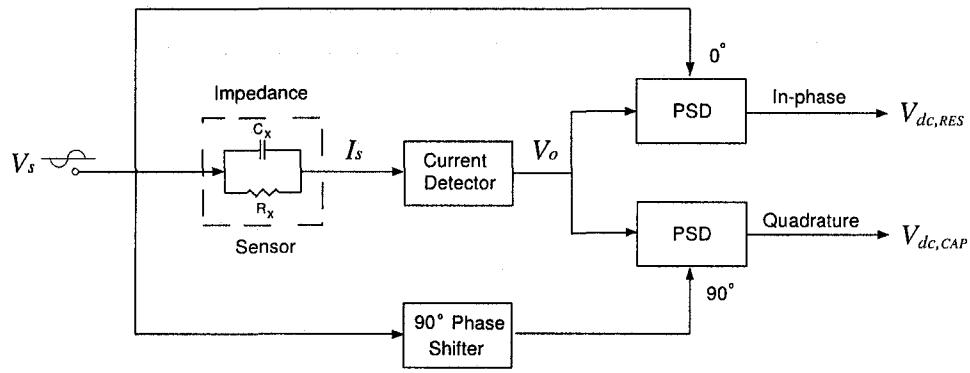

Figure 2-16: Signal detecting and demodulating schematic block diagram.

can be achieved from the quadrature PSD output ($V_{dc,CAP}$).

Demodulating Principle

A PSD schematic diagram is drawn in Figure (2-17). Assume the input signal

$$v_i(t) = \sqrt{2}V_i \cos(\omega_i t + \phi_i) \tag{2.11}$$

and the reference signal

$$v_r(t) = \sqrt{2}V_r \cos(\omega_r t + \phi_r) \tag{2.12}$$

then the output of the multiplier

$$\begin{aligned} v_p(t) &= v_i(t)v_r(t) \\ &= V_i V_r \cos[(\omega_i + \omega_r)t + (\phi_i + \phi_r)] \\ &\quad + V_i V_r \cos[(\omega_i - \omega_r)t + (\phi_i - \phi_r)] \end{aligned} \tag{2.13}$$

If these two signals are the same in frequency and phase ($\omega_i = \omega_r, \phi_i = \phi_r$), the output of the low-pass filter will be a DC component, which is proportional to the input signal V_i.

$$V_{dc} = V_i V_r \cos(0) = V_i V_r = K V_i \tag{2.14}$$

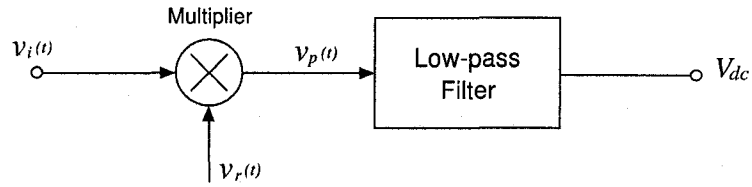

Figure 2-17: Phase-sensitive demodulator schematic diagram [19].

where $K = V_r$= Constant.

If they are the same in frequency and with quadrature difference in phase ($\omega_i = \omega_r, \phi_i = \phi_r - \frac{\pi}{2}$), the output of the low-pass filter will be zero.

$$V_{dc} = V_s V_r \cos(\frac{\pi}{2}) = 0 \tag{2.15}$$

In terms of Equation (2.14) and Equation (2.15), the corresponding DC voltage of the sensor measured conductance or capacitance can be respectively achieved by employing an in-phase or a quadrature reference signal into PSD [19].

2.4 Concluding Remarks

This chapter gives a set of background literature in the area of the multiphase flow, current multiphase flowmeter technologies, and the detection and demodulation of impedance signals. The rest of this thesis will follow the circuit theories discussed in this chapter to develop a DSP-based impedance measuring instrument.

Chapter 3

Design and Implementation of an impedance-based measuring instrument

This chapter will discuss issues and challenges that occurred in the design and implementation of the impedance-based measuring instrument. The discussion will be divided into two parts: an analog solution and a digital solution. These two methods are based on analog circuits and DSP techniques, respectively.

3.1 Analog Solution

3.1.1 An overview of the system

Figure (3-1) shows an analog detection and demodulation schematic diagram for the impedance-based measuring instrument. The system illustrated in the diagram consists of four main parts: stray-immune current detector, AC amplifier, phase-sensitive demodulators, and data acquisition card in the computer.

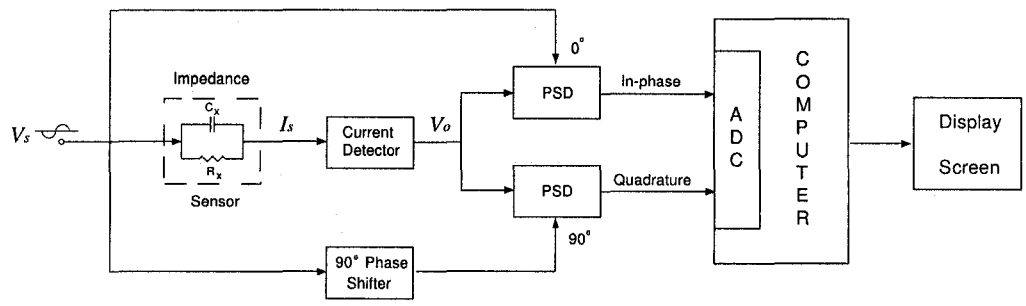

Figure 3-1: The schematic diagram for the analog detection and demodulation.

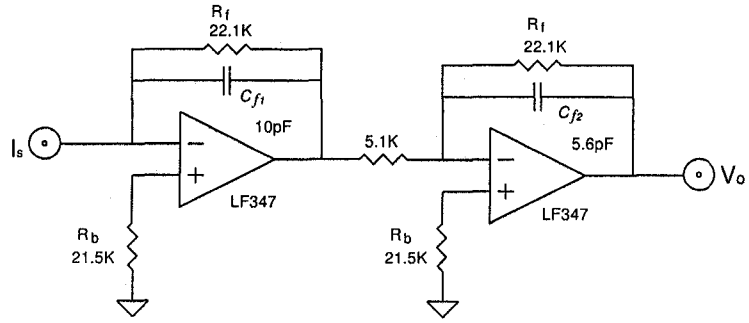

Figure 3-2: Stray-immune current detector and AC amplifier schematic diagram [20].

3.1.2 Stray-immune current detector and AC amplifier

A stray-immune current detector and an AC amplifier is illustrated in Figure (3-2), where a wide bandwidth quad JFET input operational amplifier (LF347) is employed for the current detection and amplification. Moreover, for minimizing the DC offset of the operational amplifiers, bias resistors (R_b) are used in the design, and their resistances should be slightly less than the feedback resistances (R_f). In addition, the small compensation capacitors (C_{f_1} and C_{f_2}) are used in the feedback loop to improve the dynamic responses of operational amplifiers [20].

3.1.3 Phase-sensitive demodulators (PSDs)

As shown in Figure (3-3), the PSDs used in the analog solution are composed of a phase shifter, two multipliers, two low-pass filters, and three hardware buffers. In the

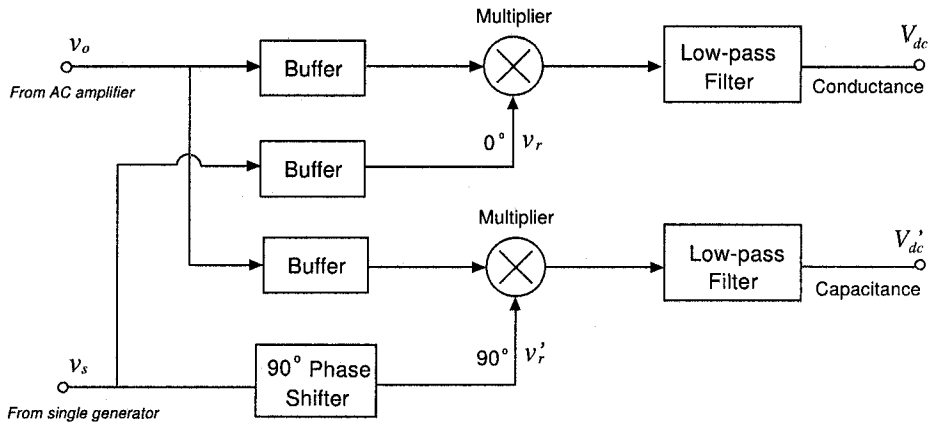

Figure 3-3: The schematic diagram for PSDs used in the analog solution.

design, multipliers and hardware buffers are easily constructed by two wide bandwidth precision analog multipliers (MPY634KP) and a wide bandwidth quad JFET input operational amplifier (LF347). However, the remaining two parts, the phase shifter and low-pass filters, are hard to implement in the circuit. Several new methods are therefore proposed in the design.

Phase shifter

As mentioned in the previous paragraph, a 90° phase shifter is required in the quadrature demodulation. The conventional analog oscillation circuit could not generate an exact 90° phase shifted signal, so the EPROM and DAC chips are used to solve this problem. However, this method is only suitable for the generation of the low frequency quadrature signals. Therefore, a new method, Direct Digital Synthesis (DDS), is proposed to generate the high frequency quadrature signals.

The principle of DDS method Figure (3-4) illustrates a schematic diagram of a DDS quadrature signal generator, which can output a sine-wave signal and a 90° phase shifted sinusoidal signal (cosine-wave). In Figure (3-5), CMOS switches, resistor networks and summers (operational amplifiers) are used to generate the 16-step sinusoidal signals in the outputs [21]. In addition, the capacitors are employed in the

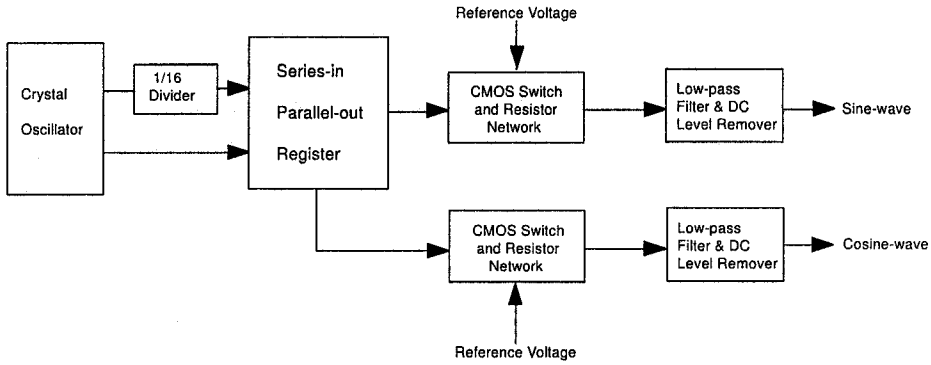

Figure 3-4: The schematic diagram of a DDS quadrature phase shifter [21], [22].

design to smooth 16-step output signals into continuous sinusoidal signals.

Figure (3-6) shows the principle of this DDS signal generator. The cosine-wave is formed by a combination of the control pulses ($Q1$, $Q2$, $Q3$, $Q4$, $Q5$, $Q6$, $Q7$ and $Q8$). The sine-wave is formed by another combination of control pulses ($Q5$, $Q6$, $Q7$, $Q8$, $\overline{Q1}$, $\overline{Q2}$, $\overline{Q3}$ and $\overline{Q4}$). The relative values of the resistors (R_1,R_2,R_3 and R_4) can be obtained by the following equations [21]:

$$\frac{1}{R_1} = \sin\frac{\pi}{8} = 0.3827 \tag{3.1}$$

$$\frac{1}{R_1} + \frac{1}{R_2} = \sin\frac{\pi}{4} = 0.7071 \tag{3.2}$$

$$\frac{1}{R_1} + \frac{1}{R_2} + \frac{1}{R_3} = \sin\frac{3\pi}{8} = 0.9293 \tag{3.3}$$

$$\frac{1}{R_1} + \frac{1}{R_2} + \frac{1}{R_3} + \frac{1}{R_4} = \sin\frac{\pi}{2} = 1 \tag{3.4}$$

For easy comparison, the relative values, desirable values and actual values of these resistors are also listed in Table (3.1).

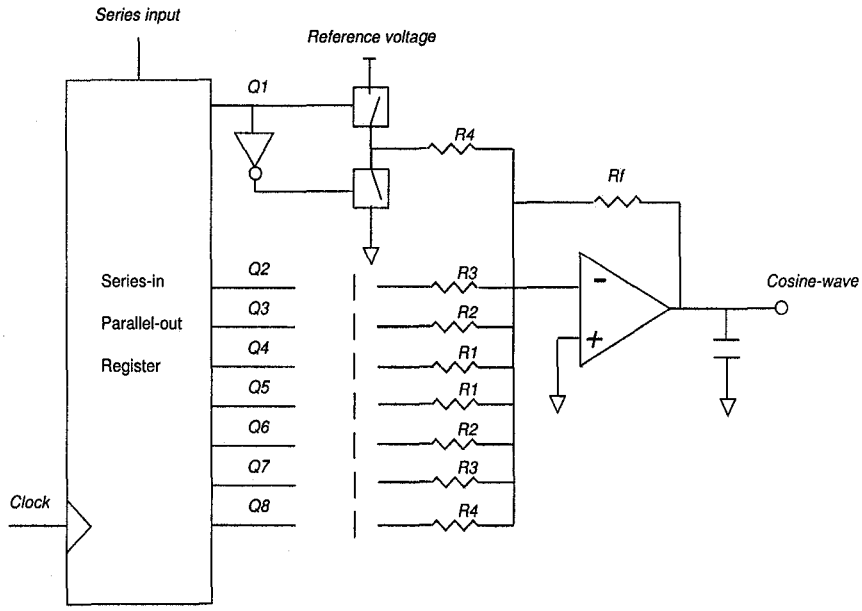

(a) Cosine-wave synthesizer circuit.

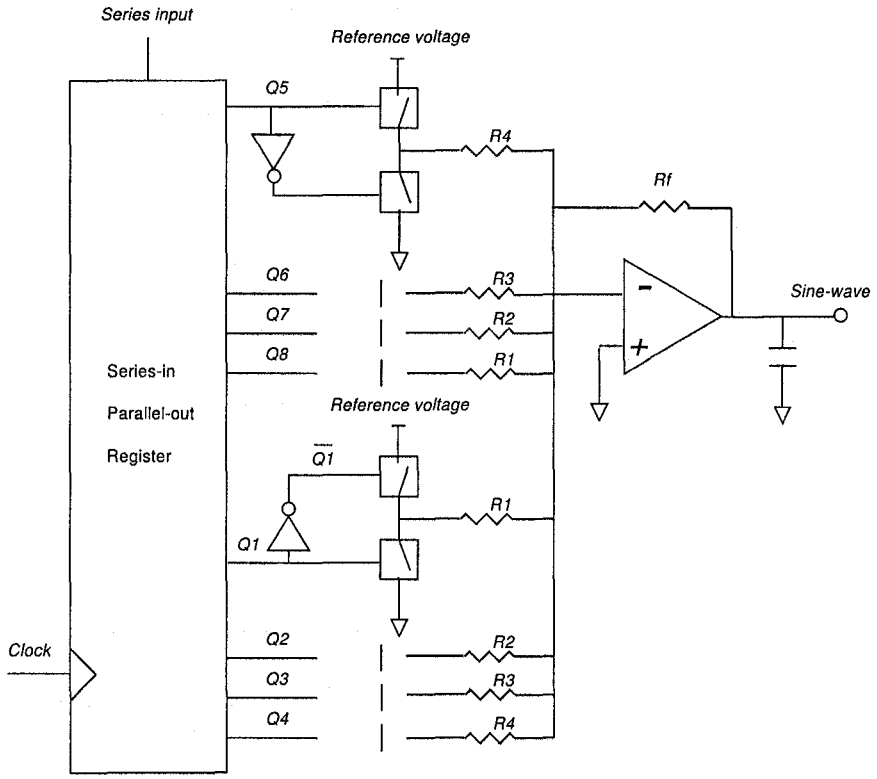

(b) Sine-wave synthesizer circuit.

Figure 3-5: The schematic diagrams for CMOS switch and resistor networks [21], [22].

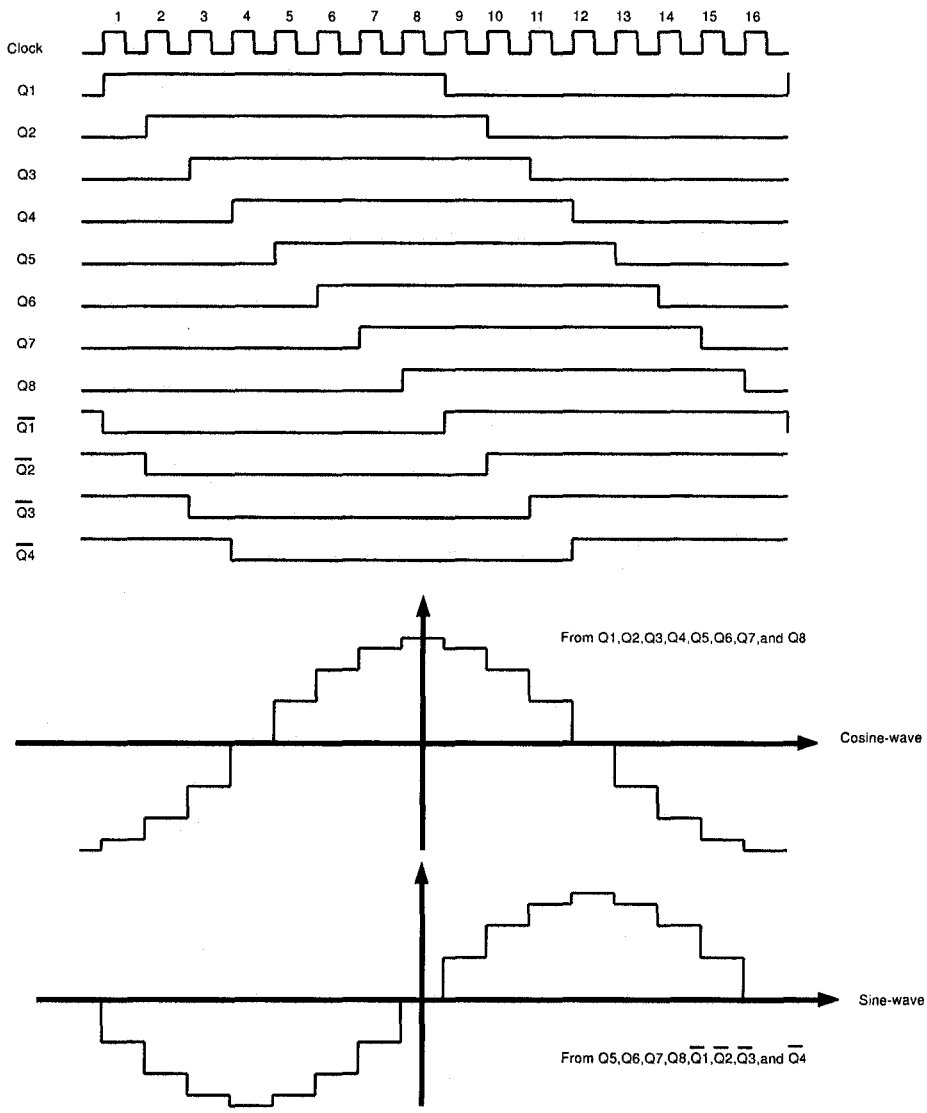

Figure 3-6: The schematic diagrams of the synthesized sine-wave and cosine-wave [21], [22].

Resistor	R_1	R_2	R_3	R_4	R_f
Relative value	2.613	3.083	4.613	13.14	
Desirable value (Ω)	1.0K	1.18K	1.77K	5.03K	382.7
Actual value (Ω)	1.0K	1.18K	1.78K	4.99K	392
Error (%)	0	0	0.56	-0.80	

Table 3.1: Resistor values for synthesis network [21]

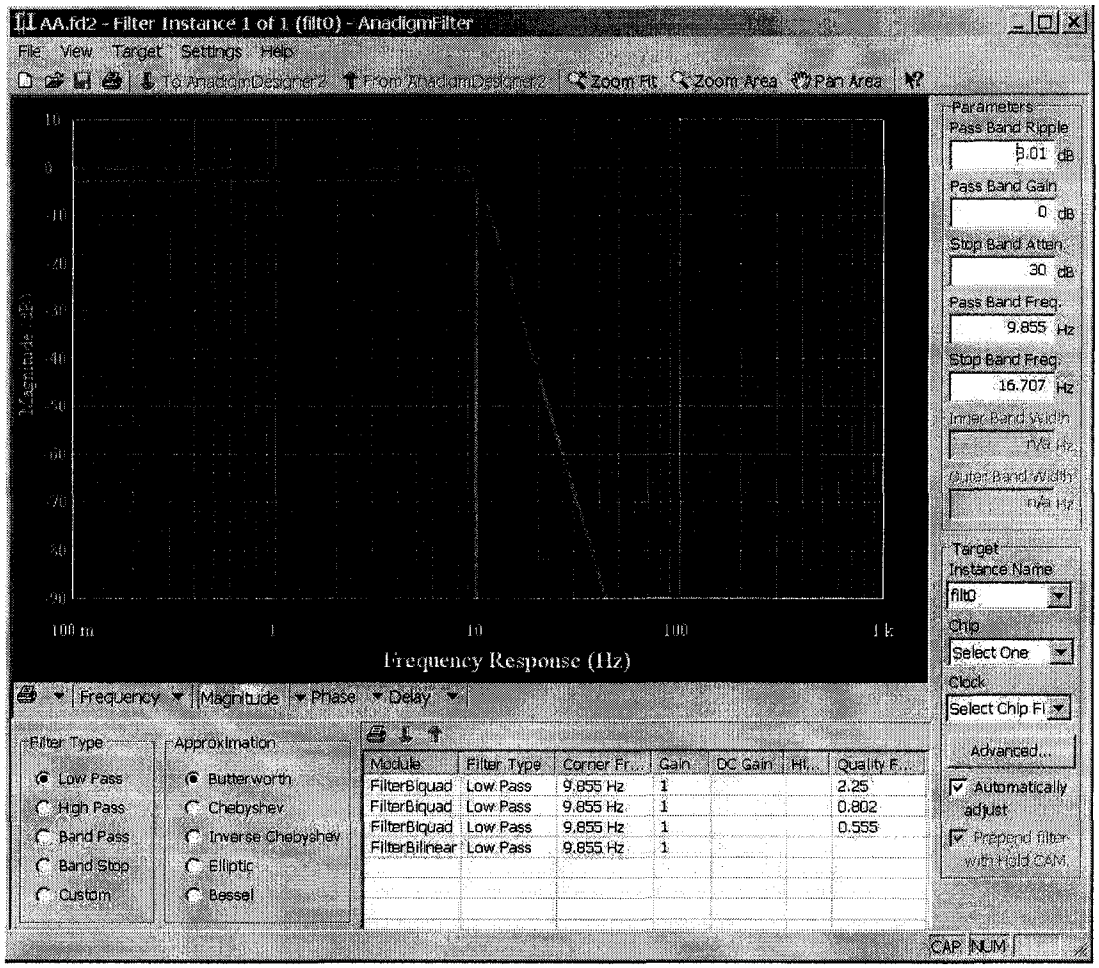

Figure 3-7: The filter setup dialog interface in Anadigm Designer2 .

Low-pass filter

The low-pass filters in the analog design are constructed by Field Programmable Analog Arrays (FPAAs) from Anadigm® [23], which can be configured to low-pass, band-pass, and high-pass filters via a setup software, Anadigm Designer2. In Figure (3-7), a Butterworth type low-pass filter is configured in which the pass-band frequency is 9.855Hz and the stop-band frequency is 16.707Hz.

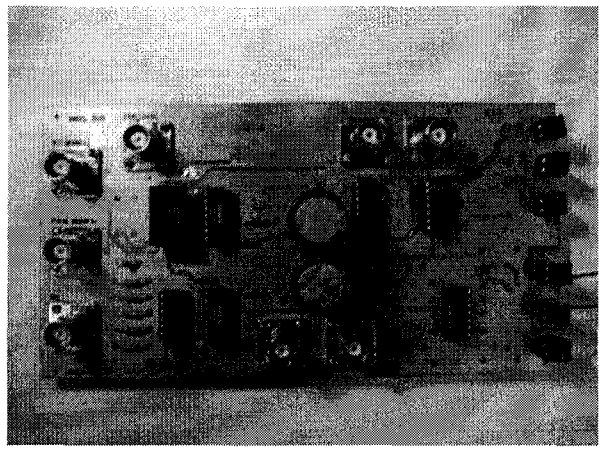

Figure 3-8: The PCB for the analog solution.

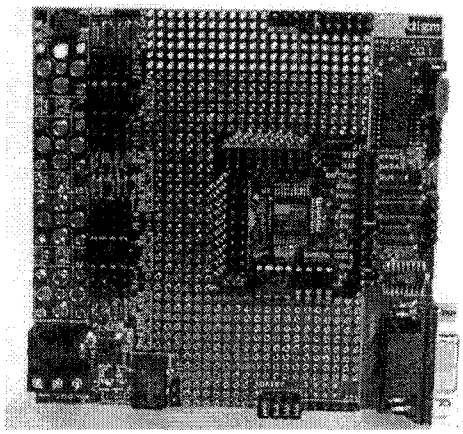

Figure 3-9: AN221K04 - Anadigmvortex development board.

3.1.4 Implementation

A printed circuit board (PCB) in Figure (3-8) has been designed to implement the signal detection and demodulation in the analog solution. It includes a current detector, an AC amplifier, a signal generator, a 90° phase shifter, and two phase-sensitive demodulators. As shown in Figure (3-9), an Anadigmvortex development board (AN221K04) from Anadigm is employed to build low-pass filters. A computer with a data acquisition card digitizes the outputs of the low-pass filters, and then analyzes and displays the results to the computer screen.

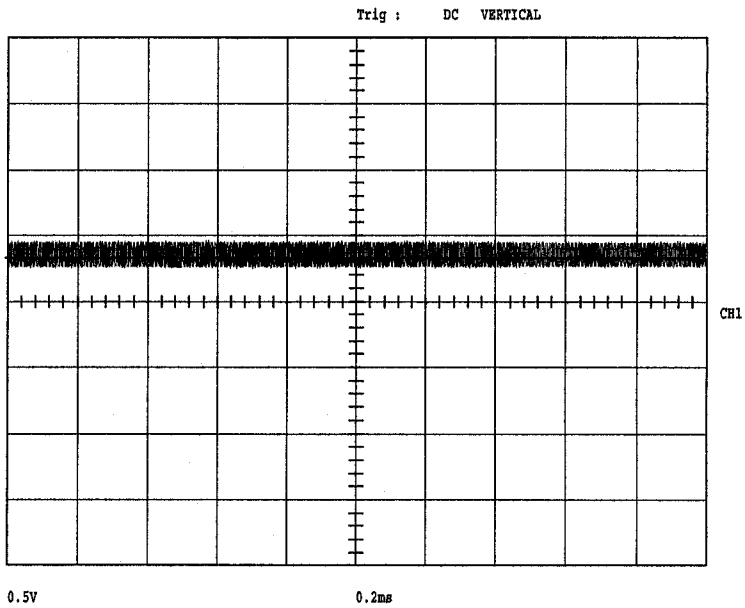

Figure 3-10: The output of the low-pass filter.

3.1.5 Results and problems

The tests show that the DC voltage outputs of the low-pass filter increase when the measured capacitances or conductances are increased, but the measuring results are not stable and no linear relationship has been obtained in the experiments. As mentioned in Chapter 2, the performance of analog PSDs is determined by the reference signals and the low-pass filters. However, the quadrature reference signal generated in this analog design was not a precise and stable 90° phase shifted signal believed to be caused by instability of analog components. Furthermore, in Figure (3-10), many high-frequency harmonics still exist in the final DC output of the low-pass filter. These unwanted ripples greatly reduced the ADC performance of the computer. In this analog implementation, the 90° phase shifter and the low-pass filters did not perform well; therefore, a digital solution was investigated as an alternative solution.

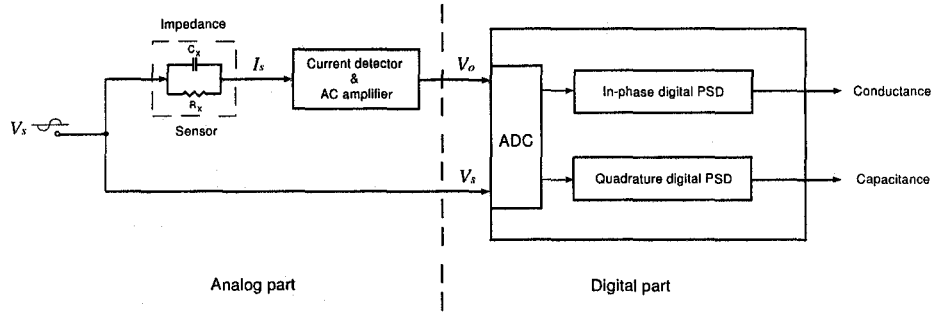

Figure 3-11: The schematic diagram for a digital solution.

3.2 Design of Digital Solution

As discussed in the previous section, the performance of analog PSDs does not meet the requirements of this research project. Therefore, a digital solution is proposed to improve the performance of signal demodulation.

3.2.1 An overview of the digital solution

Figure (3-11) illustrates a schematic diagram for the digital solution. Compared with the analog solution, the stray-immune current detector and the AC amplifier are still employed in the digital solution, whereas the PSDs are changed to digital PSDs for removing the errors from analog components. Once the ADC converts the sensor output signal (V_o) and the in-phase reference signal (V_s) into the digital sequences, the measured conductance and capacitance can be achieved by a series of numerical operations in digital PSDs.

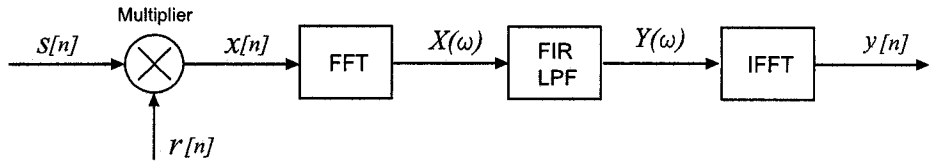

Figure 3-12: Digital PSD schematic diagram.

3.2.2 The principle of digital PSDs

The principle of digital PSDs is discussed in the following two areas.

In-phase demodulation

Figure (3-12) shows a schematic diagram of a digital PSD. $s[n]$ stands for a digital input signal sampled from the output of the AC amplifier (V_o). $r[n]$ stands for a digital reference signal sampled from the in-phase reference signal (V_s).

Thus, the output of the digital multiplier is

$$x[n] = s[n] \cdot r[n] \tag{3.5}$$

After a Fast Fourier Transform (FFT) illustrated in Figure (3-12), the time domain digital signal $x[n]$ is transfered into the frequency domain digital signal $X(\omega)$. Figure (3-13) shows that the frequency characteristic of $X(\omega)$ is in accordance with the theoretical analysis in Equation (2.13). Namely, when two signals with the same frequency are multiplied together, a DC component and a component with twice the frequency will be generated in the output signal.

Next, a digital finite impulse response (FIR) low-pass filter is designed to remove the high-frequency component from $X(\omega)$, so a DC frequency domain signal $Y(\omega)$ can be obtained by

$$Y(\omega) = X(\omega) \cdot H(\omega) \tag{3.6}$$

where $H(\omega)$ is the frequency response function of the FIR low-pass filter. The perfor-

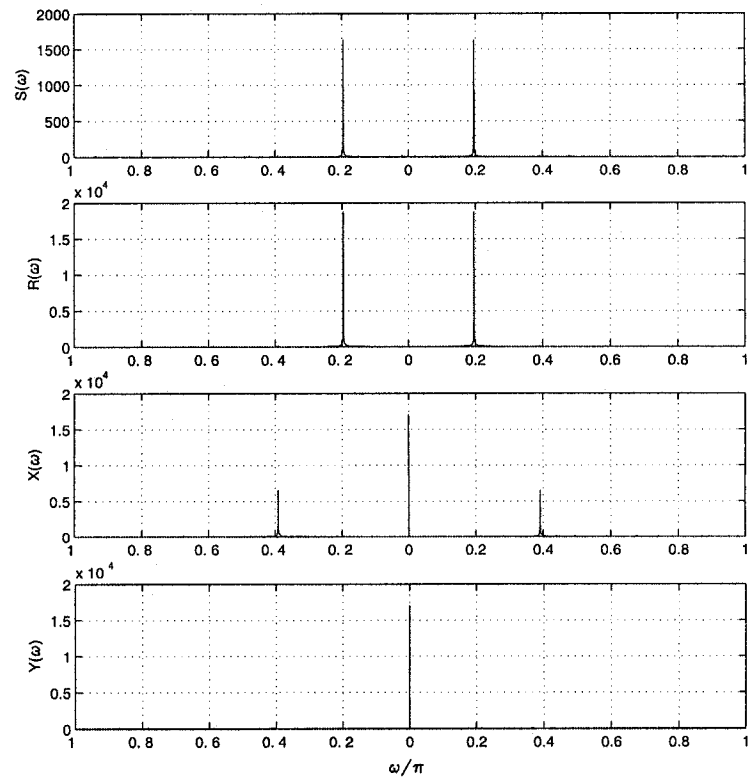

Figure 3-13: The magnitude of the input and output of the digital multiplier.

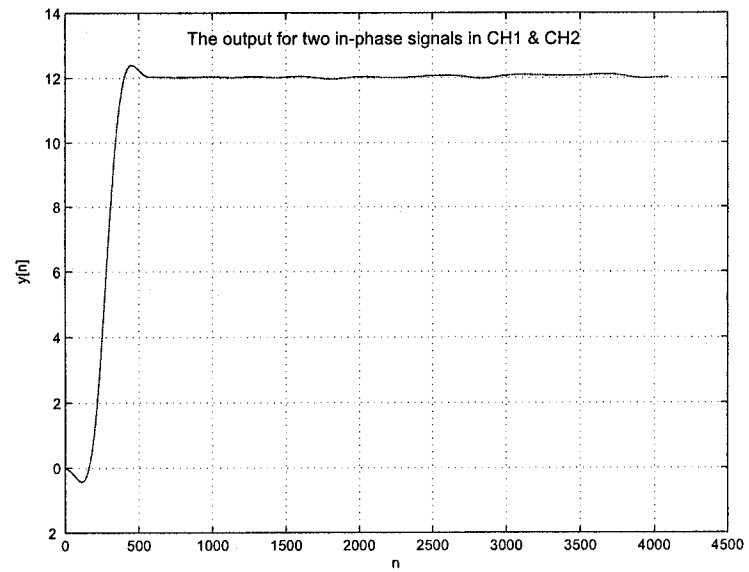

Figure 3-14: The output y[n] of the in-phase digital PSD.

mance of this FIR filter is also shown in Figure (3-13), where only the DC component is left in the $Y(\omega)$, which is much better than the performance of the analog low-pass filter.

Finally, the time domain DC signal y[n] (namely, the output of the digital PSD) is achieved by employing an inverse FFT to $Y(\omega)$. In Figure (3-14), a very straight line is obtained except for initial transitions, which means that a stable DC component is obtained in the output of the digital PSD. Therefore, the digital PSD can be employed in the in-phase demodulation.

Quadrature demodulation

A highly precise and stable 90° phase-shifted reference signal is difficult to obtain in the analog circuit. However, it can be implemented in the digital PSD with less complex techniques. A sinusoidal time domain signal and its corresponding frequency domain signal are shown in Equation (3.7).

$$\cos(\omega_0 n + \phi) \Longrightarrow \pi e^{j\phi}\delta(\omega - \omega_0) + \pi e^{-j\phi}\delta(\omega + \omega_0) \tag{3.7}$$

where $\omega \in (-\pi, \pi)$.

Assume an in-phase reference signal $r[n] = \cos(\omega_0 n + 0)$ and a 90° phase-shifted reference signal $r'[n] = \cos(\omega_0 n + \frac{\pi}{2})$. Then, the frequency responses of $r[n]$ and $r'[n]$ are

$$R(\omega) = \pi\delta(\omega - \omega_0) + \pi\delta(\omega + \omega_0) \tag{3.8}$$

$$R'(\omega) = j\pi\delta(\omega - \omega_0) - j\pi\delta(\omega + \omega_0) \tag{3.9}$$

where $\omega \in (-\pi, \pi)$.

In comparison with Equation (3.8) and Equation (3.9), one "−" sign and two "j" are the only differences between them. Thus, $R'(\omega)$ can be easily achieved from $R(\omega)$ after several simple math calculations. Furthermore, the quadrature reference $r'[n]$ can be obtained by employing an inverse FFT to $R'(\omega)$.

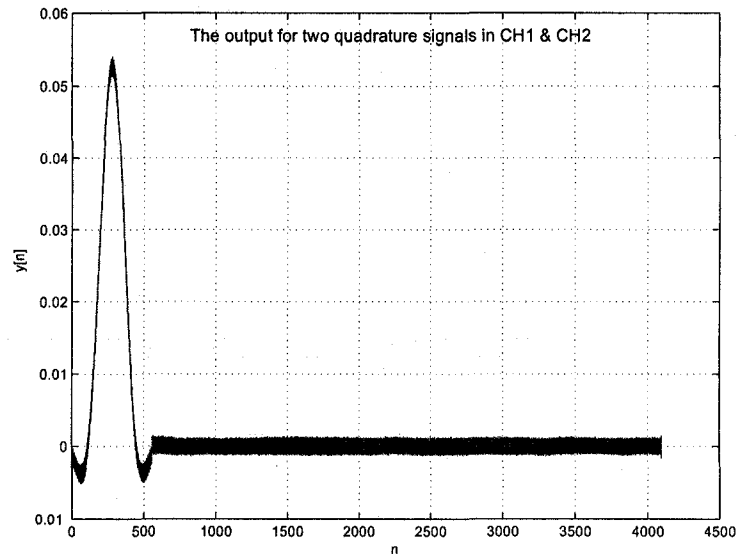

Figure 3-15: The output y[n] of two quadrature signals.

In Figure (3-15), two quadrature digital sequences $r[n]$ and $r'[n]$ are fed into the digital PSD. The output y[n] is close to zero except for initial transitions. This is in accordance with the quadrature demodulating formula in Equation (2.15). Therefore, this $r'[n]$ is a precise and stable 90° phase-shifted reference signal and the generating method presented above is correct.

Once a 90° phase-shifted reference signal $r'[n]$ is obtained, the rest procedures for the quadrature digital PSD are the same as those of the in-phase digital PSD (namely, $x'[n] = s[n] \cdot r'[n]$), which has been illustrated in Figure (3-12). Finally, a similar straight line in Figure (3-14) is achieved by the quadrature digital PSD. Therefore, this digital PSD can be employed in the quadrature demodulation.

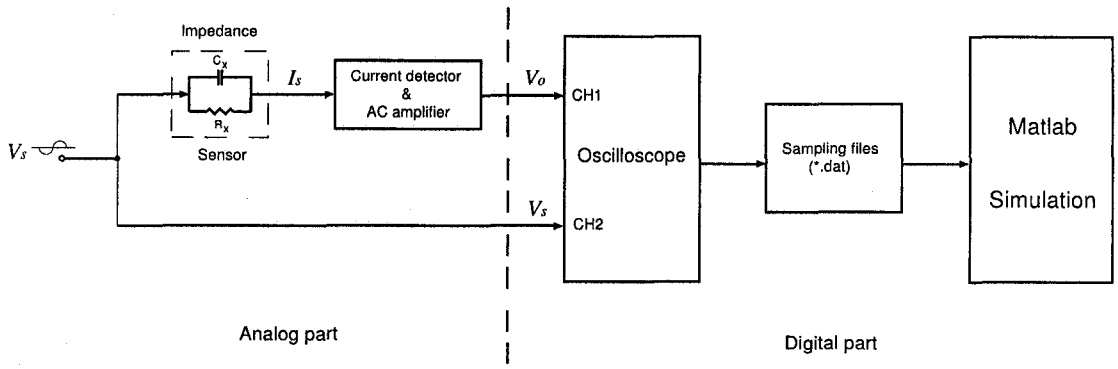

Figure 3-16: The schematic diagram for simulations in Matlab.

3.2.3 Simulations in Matlab

In this thesis, several simulations in Matlab are performed to verify the DSP concepts mentioned in the previous subsection. A schematic diagram of the simulation system is shown in Figure (3-16), where a Tektronix 2212 storage oscilloscope is used for data acquisition. At first, the sensor output signal V_o and the in-phase input signal V_s are sampled into data file by CH1 and CH2 of the oscilloscope. Then, this data will be analyzed by the simulation program in Matlab.

According to the Nyquist sampling theorem, the sampling rate is at least twice as fast as the maximum signal frequency ($f_s \geq 2f_{max}$). In order to avoid the aliasing in the samples and improve the sampling performance, the sampling frequency in this research project is chosen to be ten times faster than the maximum signal frequency ($f_s \geq 10f_{max}$).

As shown in Figure (3-16), the digital PSDs are realized by the simulation program in Matlab. This simulation program can read sampling data file from the oscilloscope, and then follow the digital processes illustrated in Figure (3-12). At the final stage of the digital processes, a digital sequence y[n] can be achieved. For easy comparison with the other measuring data, the mean of y[n] is adopted for the final output of the digital PSD in this thesis.

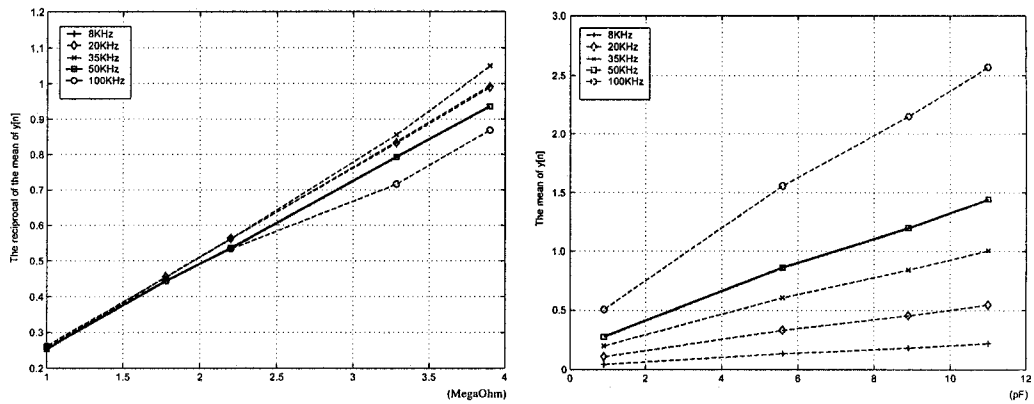

(a) Conductance (b) Capacitance

Figure 3-17: The impedance measuring results in different frequencies.

The theoretical analysis in Equation (2.10) shows that the current flowing through a resistor is proportional to the conductance, regardless of the signal frequency applied on the resistor ($i \propto \frac{1}{R}$). However, the current flowing through a capacitor is proportional to the product of the capacitance and the frequency applied on the capacitor ($i \propto \omega C$).

This analysis has been confirmed by the simulations in Matlab. Figure (3-17) shows the results of these simulations, where the simulations are performed in five different frequencies, 8KHz, 20KHz, 35KHz, 50KHz and 100KHz. As shown in Figure (3-17b), increasing the signal frequency can increase the accuracy of the capacitance measuring. However, too high frequency also decreases the linearity of the measuring results due to the frequency bandwidth of the analog components. With the tradeoff between the accuracy and the linearity, a 50KHz signal frequency is selected in the experiments. Consequently, the sampling rate is set to 500K samples per second.

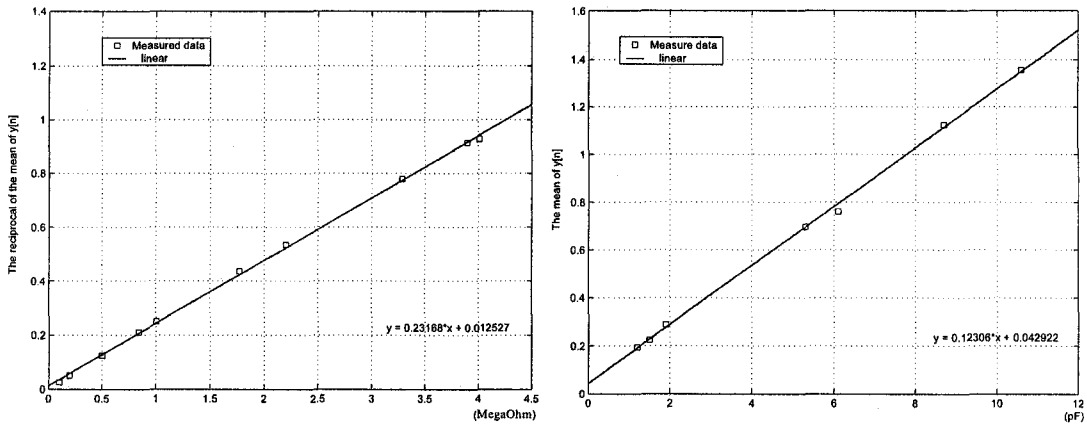

(a) Conductance (b) Capacitance

Figure 3-18: The linearity of the measuring circuit output.

Results

The experiments were conducted at 50KHz to find the regression models for the conductance and capacitance measurements. Figure (3-18a and 3-18b) show the linear relationships between simulated impedances and measured impedances in the conductance and capacitance measurements.

The linear regression models are given as:

$$\frac{1}{\overline{y}[n]} = 0.23168 \times \text{Resistance} + 0.012527 \tag{3.10}$$

$$\overline{y}[n] = 0.12306 \times \text{Capacitance} + 0.042922 \tag{3.11}$$

where

$\overline{y}[n]$ is the mean of the output y[n] of the digital PSD.

In Figure (3-18), the correlation coefficients between the measured impedances and the simulated impedance are greater than 0.999. In other words, this digital method has good linearity in the conductance and capacitance measurements.

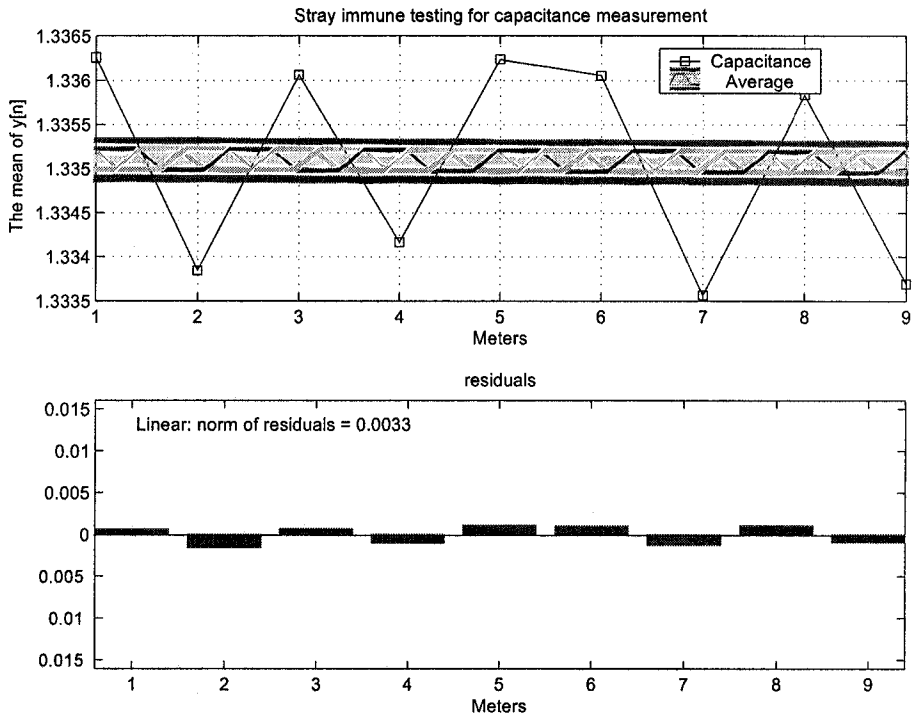

Figure 3-19: The results for the stray-immune tests of the measuring circuit.

Stray-immune tests

Stray-immune is a necessary characteristic for the research in this thesis because long cables assumed to be used between the subsea electrodes and the topside field electronics can generate large stray capacitances in the measurement. In order to verify this characteristic, stray-immune tests were performed when the different length of cables were connected between the output of the sensor and the input of the current detector. In Figure (3-19), the testing results show that the measured capacitances (the means of y[n]) have a low dispersion and the norm of residuals is small to 0.0033, which is in accordance with the theoretical analysis in Chapter 2. As a result, the measuring circuit used in this research have a stray-immune characteristic.

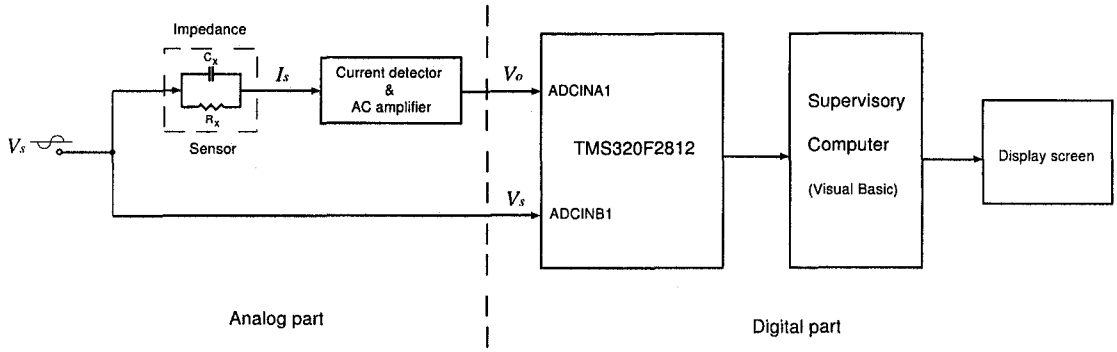

Figure 3-20: The schematic diagram of a DSP-based impedance measuring system.

3.3 Implementation of Digital Solution

After successful simulations in Matlab, a digital signal processor (TMS320F2812) is introduced to perform data acquisition and digital data analysis in the design. In contrast to the offline impedance data obtained in Matlab simulations, this DSP chip can provide real-time impedance data in the measurement.

3.3.1 A overview of DSP system

Figure (3-20) illustrates a schematic diagram of this DSP-based measuring system. In TMS320F2812, two ADC input channels (ADCINA1 and ADCINB1) sample the sensor output signal V_o and the in-phase input signal V_s simultaneously. After digital signal processes in TMS320F2812, the measuring results can be transmitted to a supervisory computer via serial communication interface (SCI). In addition, a Visual Basic (VB) management program has been developed to implement the serial communication, data display and data analysis for the supervisory computer.

3.3.2 TMS320F2812 and eZdsp^{TM} F2812

The digital signal processor TMS320F2812 is made by Texas Instruments. It offers 150 MIPS, 32-bit DSP performance, and provides 16-channel, 12-bit ADC with up to 12.5 MSPS conversion speed [11].

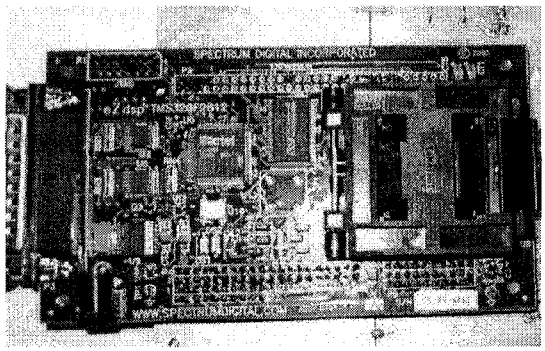

(a) Development board

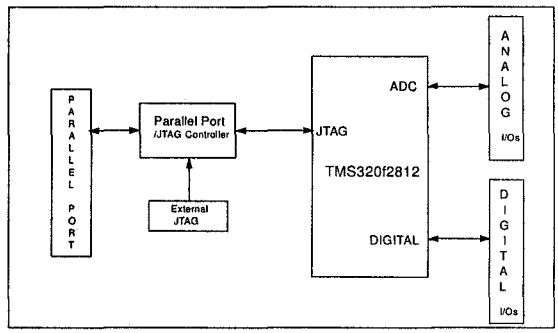

(b) Block diagram [24]

Figure 3-21: The eZdsp^{TM} F2812 development board.

For easy implementation, a DSP development board, eZdsp^{TM} F2812 from Spectrum Digital, is chosen in the thesis. The top view and the block diagram of this development board are shown in Figure (3-21). This board integrates a digital signal processer (TMS320F2812) and the digital/analog I/O interfaces. In addition, the communication between the TMS320F2812 and the programming computer is implemented by an embedded IEEE 1149.1 JTAG controller on the development board via a parallel interface.

3.3.3 Hardware implementation

Like the digital simulations mentioned in the previous section, the stray-immune current detector is still in the analog circuit. However, in this DSP circuit, the AC amplifier is changed to a digitally-controlled programmable-gain instrumentation amplifier (PGA203), which provides gains of 1, 2, 4, and 8 and can be controlled by the DSP microprocessor.

Voltage level shifter

The sensor output signal V_o and the in-phase input signal V_s are bipolar signals, with a range between -1.5V and +1.5V. However, the ADC input channels (ADCINA1 and

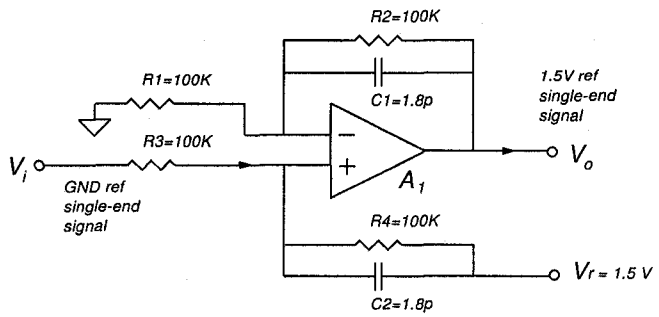

Figure 3-22: The +1.5V voltage level shifter [25].

ADCINB1) of TMS320F2812 require unipolar signals between 0V and 3V. Therefore, two voltage level shifters are needed in the F2812 ADC processes. Figure (3-22) illustrates a +1.5V voltage level shifter. Since the opamp input currents are zero ($i_+ = i_- = 0$), and opamp input voltages are the same (V_+=V_-), two nodal equations can be obtained

$$\frac{0 - V_-}{R_1} + \frac{V_o - V_-}{Z_1} = 0 \tag{3.12}$$

$$\frac{V_i - V_+}{R_3} + \frac{V_r - V_+}{Z_2} = 0 \tag{3.13}$$

where $Z_1 = \frac{R_2}{1+j\omega C_1 R_2}$, $Z_2 = \frac{R_4}{1+j\omega C_2 R_4}$

In terms of the values of resistors and capacitors in Figure (3-22)

$$Z_1 = Z_2 \approx R1 \tag{3.14}$$

Thus, Equation (3.12) and Equation (3.13) can be solved as

$$V_o = V_i + V_r = V_i + 1.5 \tag{3.15}$$

Therefore, the bipolar input signal V_i (-1.5V $\sim$ +1.5V) is shifted to the unipolar output signal V_o (0V $\sim$ +3V).

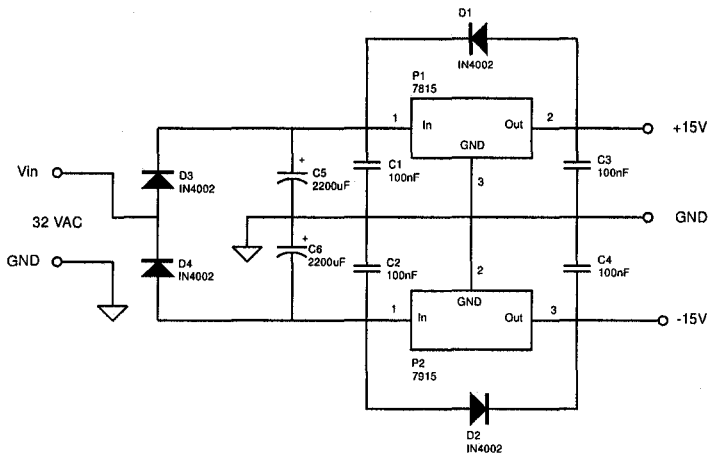

(a) +15V and -15V

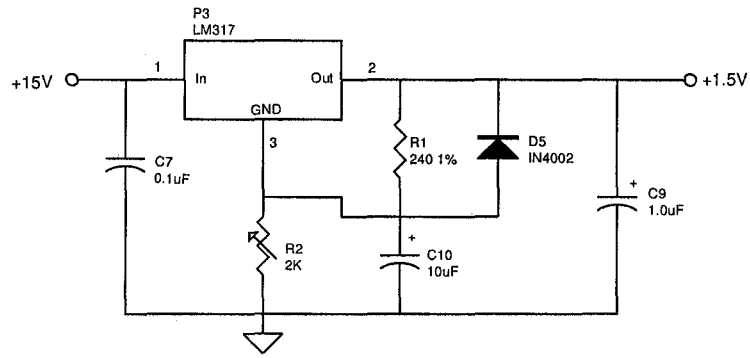

(b) +1.5 Reference voltage

Figure 3-23: The schematic diagram for the power supply.

Power supply

In this thesis, the power supply is designed to provide +15V, -15V, and the reference voltage +1.5V. Figure (3-23a) shows the schematic diagram of a dual-output power supply, where the regulators 7815 and 7915 are used to generate +15V and -15V. In order to generate a stable +1.5V reference voltage for the voltage level shifter, a precise voltage regulator (LM317) is employed in the design, and its schematic diagram is illustrated in Figure (3-23b). Note that the output voltage of LM317 can also be adjusted from 1.2V to 37V by tuning a variable resistor R_2.

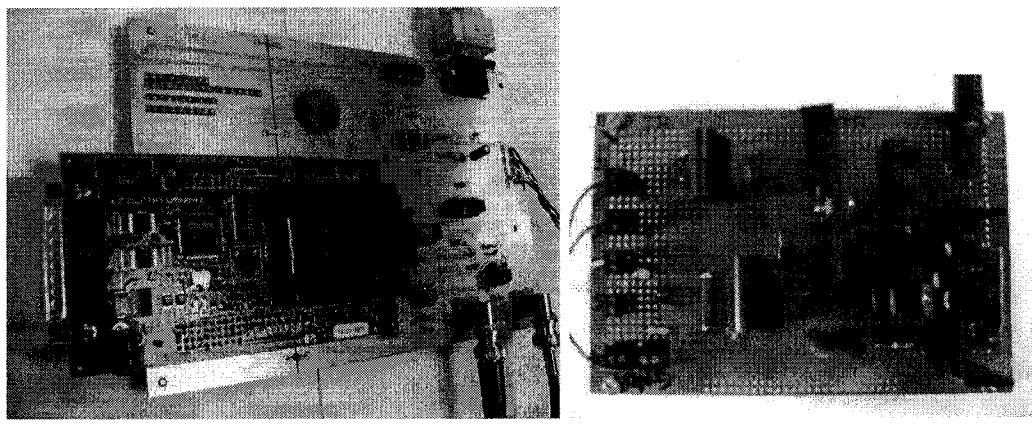

(a) Signal conditioning board (b) Power supply

Figure 3-24: The pictures of the signal conditioning board and the power supply.

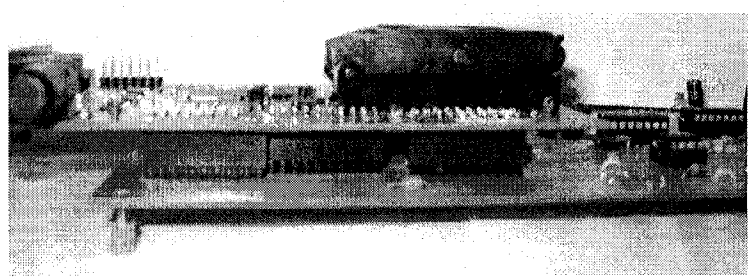

Figure 3-25: The side view of the eZdsp^{TM} F2812 and the signal conditioning board.

DSP signal conditioning board

As shown in Figure (3-24), a DSP signal conditioning board has been designed and constructed to integrate the stray-immune current detector, the instrumentation amplifier, the voltage level shifters, the serial communication voltage convertor (MAX3232), and the eZdsp^{TM} F2812 development board together. In Figure (3-25), the eZdsp^{TM} F2812 development board is overlapped on the top of the signal conditioning board, which is known as the daughter card design. The detail schematic and PCB layout diagrams will be listed in Appendix A.

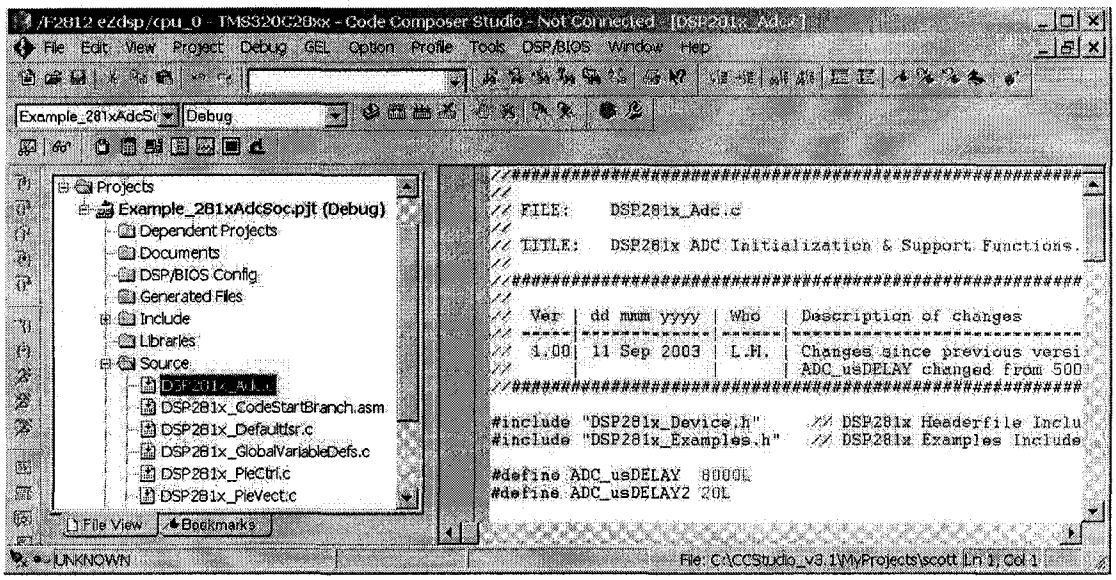

Figure 3-26: The software interface of Code Composer Studio ^{TM} IDE.

3.3.4 Software implementation

In this thesis, a C-language control program and a VB management program have been developed for the digital signal processor (TMS320F2812) and the supervisory computer, respectively. The C program is in charge of data acquisition and DSP analysis, and the VB program conducts the data display and the further data statistics.

Code Composer Studio^{TM} IDE

It should be noted that only an assembly language program can be run in the TMS320F2812. Therefore, a C-compiler software, Code Composer Studio ^{TM} IDE from Texas Instruments, is used to compile a C-language program to an assembly language program. As shown in Figure (3-26), the code editor, debugger, compiler, and linker are all included in this software integrated development environment.

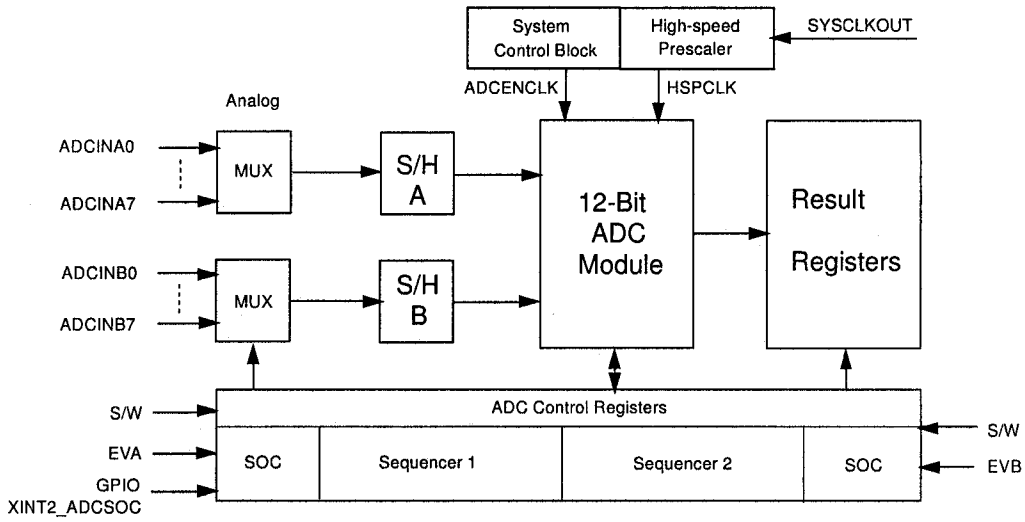

Figure 3-27: The block diagram of ADC module [26].

The C program for TMS320F2812

A multi-thread technique is applied to this control program to perform data acquisition and DSP analysis simultaneously. Therefore the whole control program is divided into two parts: the main routine and the interrupt routines. Namely, the DSP analysis is run in the main routine; and data acquisition is performed in the ADC interrupt subroutine. In addition, the serial communication program is written in the SCI interrupt subroutine.

ADC setup Figure (3-27) shows a block diagram of the ADC module in TMS320F2812. 16 ADC channels are divided into two groups: Group A and Group B. Each group has an analog MUX to switch different inputs to the sampling holder (S/H). These two groups can be operated in the sequential sampling mode or the simultaneous sampling mode. For this thesis, the simultaneous sampling mode is chosen to obtain the sensor output signal V_o and the in-phase input signal V_s at the same time.

The parts of the program codes of the ADC process are written in the following paragraph. As discussed in Matlab simulations, the sampling rate is set to 520KHz, which is 10 times faster than the maximum signal frequency 50KHz. The sampling

results stored in the registers have 12 significant bits and they are MSB aligned. Therefore, a 4-bit right shift is needed when they are read in the program.

```
AdcRegs.ADCTRL3.bit.ADCCLKPS=3;
          // ADCCLK=HISPCLK/(2*ADCCLKPS)=25/6=4.16667MHz
AdcRegs.ADCTRL1.bit.ACQ_PS=0x7;
          // The width of SOC pulse is (ACQ_PS +1) ADC_CLK
          // HERE, 0x7 should be 8 ADC_CLK width. //  520KHz
AdcRegs.ADCTRL3.bit.SMODE_SEL = 1;       // Simultaneous mode
AdcRegs.ADCMAXCONV.all = 0;
AdcRegs.ADCCHSELSEQ1.bit.CONV00 = 0x0;
// Enable SEQ1 interrupt (every EOS)
AdcRegs.ADCTRL2.bit.INT_ENA_SEQ1 = 1;

// Setup continuous run
AdcRegs.ADCTRL1.bit.CONT_RUN = 1;
// Start ADC Sampling SEQ1
AdcRegs.ADCTRL2.bit.SOC_SEQ1 = 1;

Voltage1[ConversionCount] = AdcRegs.ADCRESULT0 >>4;
Voltage2[ConversionCount] = AdcRegs.ADCRESULT1 >>4;
```

SCI setup The communication between the microprocessor and the supervisory computer is based on a serial communication interface (RS232). The parts of the program codes of the SCI process will be shown in the following paragraph, where the communication control mode is set to 19200 baud, one stop bit, no parity, 8-bit char, and asynchronous mode. In TMS320F2812, the transmit FIFO and receive FIFO buffers both have 16 words in length. The second "2" in the SCI FIFO receive register (SCIFFRX) means a receive FIFO interrupt will be generated once two words

are received by the receive FIFO buffer. However, the "4" in the SCI FIFO transmit register (SCIFFTX) does not mean a transmit FIFO interrupt will be generated when four words are written into the transmit FIFO buffer, but a transmitting interrupt occurs once 12 words are written into FIFO buffers ($16 - 4 = 12$).

```
SciaRegs.SCICCR.all =0x0007;
   // 1 stop bit,  No loopback, No parity, 8-bit char.
SciaRegs.SCICTL1.all =0x0003;
   // enable TX, RX, internal SCICLK.
SciaRegs.SCIHBAUD = 0x0000;
SciaRegs.SCILBAUD =243;//(19200)
SciaRegs.SCIFFRX.all=0x0022;
   // -- receive 2 words, generate an interrupt
SciaRegs.SCIFFTX.all=0xC024;
   // (4 = 16-12)-- send 12 words, generate an interrupt
SciaRegs.SCIFFCT.all=0x00;
```

Main routine The system clock, the interrupt vectors, the entrance addresses of the interrupt service subroutine, and the interrupt enable registers must be set up at the beginning of the main routine. Then, a signal processing subroutine is run all the time, where the digital I/O operations, FFT, and IFFT are performed respectively.

GPIO The digital I/O and the peripheral I/O share the same group of pins, so they are called General Purpose Input/Output (GPIO). The block diagram of a GPIO pin is shown in Figure (3-28). When a pin is chosen as a digital I/O, its corresponding bit in the GPIO MUX register is set to "0" . Furthermore, the control bit in the GPIO DIR register should be assigned to "0" for the input or "1" for the output. The example codes are listed in the following paragraph, where 16 pins in the GPIO A group are all set to digital I/Os, and GPIOA0 and GPIOA1 are employed as the outputs to control the gain of the instrumentation amplifier.

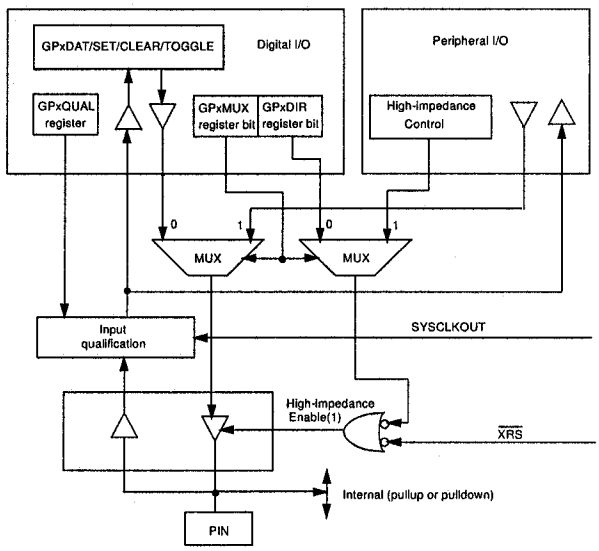

Figure 3-28: The block diagram for GPIO/Peripheral Pin MUXing [27].

```
GpioMuxRegs.GPAMUX.all=0x0000;      // DI/DO mode
GpioMuxRegs.GPADIR.all=0x0003;      // GPIOA0 and GPIOA1 as outputs
```

FFT The Fast Fourier Transform function in the Code Composer Studio ^{TM} IDE is not as simple as the FFT function in Matlab because the TMS320F2812 does not support the complex operations. N-point complex sequences have to be stored as 2N-point real sequences in the memory, which are shown in Figure (3-29).

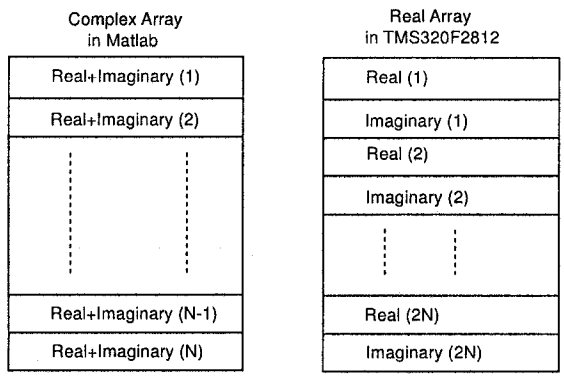

Figure 3-29: The complex FFT in TMS320F2812.

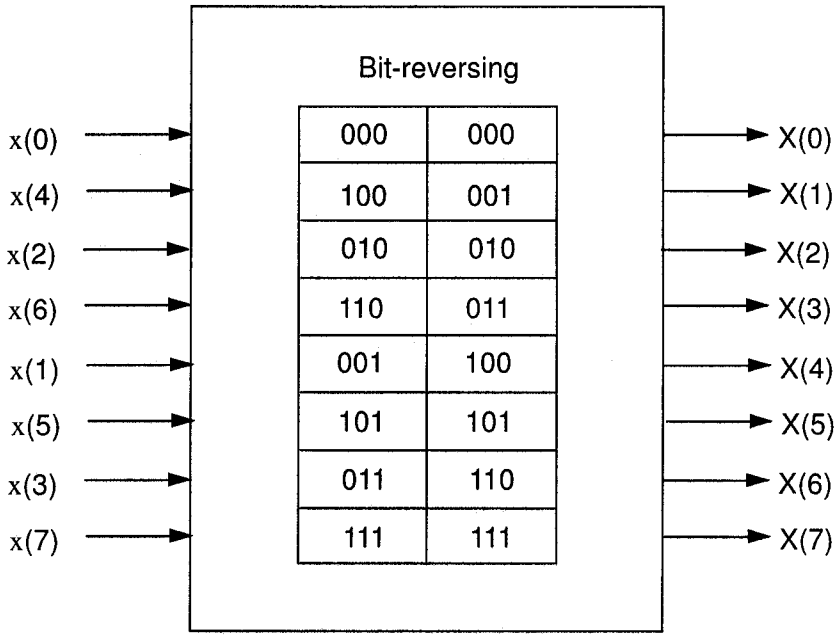

Figure 3-30: FFT flow graph for N=8 point.

Moreover, in order to store the FFT output sequence $X(k)$ in contiguous memory spaces, the input sequence $x(n)$ should be reordered by a bit-reversing operation before the FFT. For example, a FFT flow graph for 8-point sequence is illustrated in Figure (3-30). On the right side, the output sequence $X(k)$ is followed by sequential order $\{X(0), X(1), X(2), X(3), X(4), X(5), X(6), X(7)\}$, whereas on the left side, the input sequence $x(n)$ is arranged to bit-reversing order $\{x(0), x(4), x(2), x(6), x(1), x(5), x(3), x(7)\}$.

In addition, the TMS320F2812 does not provide a floating-point operation but a 32-bit fixed-point operation; therefore, for improving the accuracy of the FFT calculation, the values of the input sequences $x(n)$ should be assigned in the range of $(2^{12} \sim 2^{16})$.

IFFT The inverse FFT is not included in the Code Composer Studio ^{TM} IDE. However, the inverse FFT can be performed by a FFT [28]. Assume $x(n)$ is a real input sequence $\{x(0), x(1), x(2), x(3), \cdots, x(N)\}$. (Note that the input sequences are all real data in this thesis.)

Let

$$Y(k) = \text{FFT}(x(n)) \tag{3.16}$$

where $k \in [0, N)$, $n \in [0, N)$, $Y(k)$ is Complex.

Then

$$x'(k) = \text{FFT}(Y(k)/N) \tag{3.17}$$

where $x'(k) = \{x(0), x(N-1), x(N-2), x(N-3), \cdots, x(1)\}$.

As shown in Equation (3.17), the sequence $x'(k)$ is the time-inverse sequence of $x(n)$ except for the first element in the sequence. Therefore, the inverse FFT can obtained by Equation (3.17) and a series of reordering operations.

Memory mapping The programs run in the microprocessor are always limited by the memory spaces in the microprocessor. TMS320F2812 can reach 4M words programme and data memory spaces, but most memory spaces are reserved by the system itself. As illustrated in Figure (3-31), only 18K words memory spaces are left for users' programmes and data. Therefore, the programmer must take care of the memory usage in the program; otherwise, the unwanted overflows will occur in the program running.

In the Code Composer Studio ^{TM} IDE, a linker command file (*.CMD) is used to manage these 18K words memory spaces and the other reserved memory spaces. For example, the FFT operation needs at least three continuous memory spaces to store the in-place computation results, the magnitude of FFT, and the window of FFT. If they are not assigned in the linker command file, the system may automatically assign them in the available memory spaces. However, these assigned memory spaces

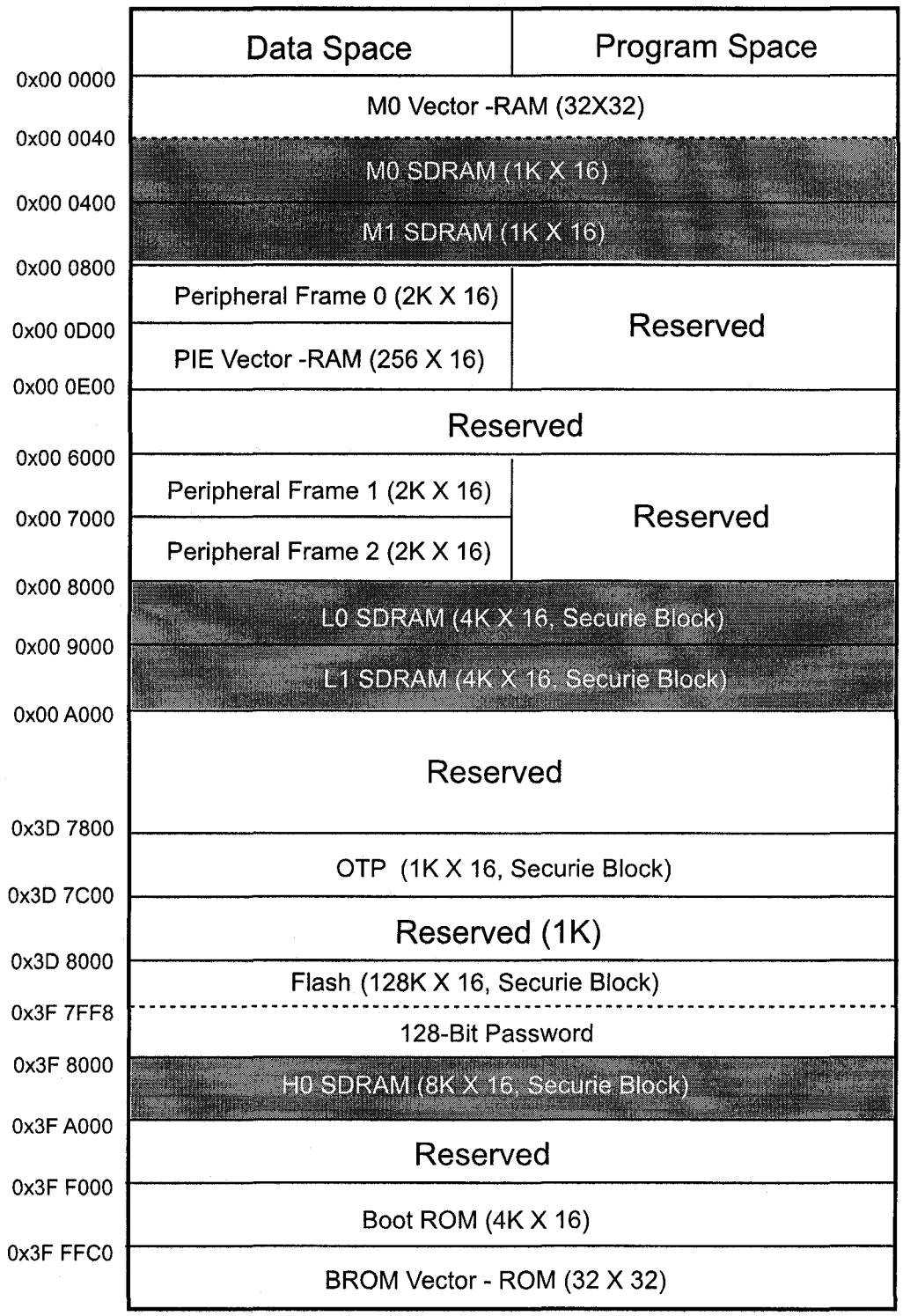

Figure 3-31: The map of the on-chip memory in TMS320F2812 [11].

are not continuous. Therefore, memory mapping process must be carried on the main program and the linker command file. The sample codes are listed in the following paragraph.

```
/* FFT memory assignment in the main program file */
#pragma DATA_SECTION(ipcb, "FFTipcb");
#pragma DATA_SECTION(mag, "FFTmag");
#pragma DATA_SECTION(win, "FFTwin");

/* FFT Locations in the linker command file */
FFTipcb ALIGN(1024): {}> RAML0L1, PAGE = 1
FFTmag > RAML0L1, PAGE = 1
FFTwin > RAML0L1, PAGE = 1
```

The Visual Basic program for supervisory computer

A VB program has been developed for data communication and management, and its interface picture is shown in Figure (3-32). As mentioned in the previous subsections, the supervisory computer acquires the measured data from the eZdspF2812 via a RS232 communication. The communication used in this thesis is based on a master/slave protocol. Namely, the master node sends a request ("Address + Command") to the network, then all the slave nodes on the network receive this request, but only one node named as that address sends back a reply with the requested data ("Command + Data"). The sample codes for the master node and the slave nodes are shown below.

```
//Sending a request in the master node
If bSending = 0 Then
   varOut = "1C"    ' address 01 , capacitance data
```

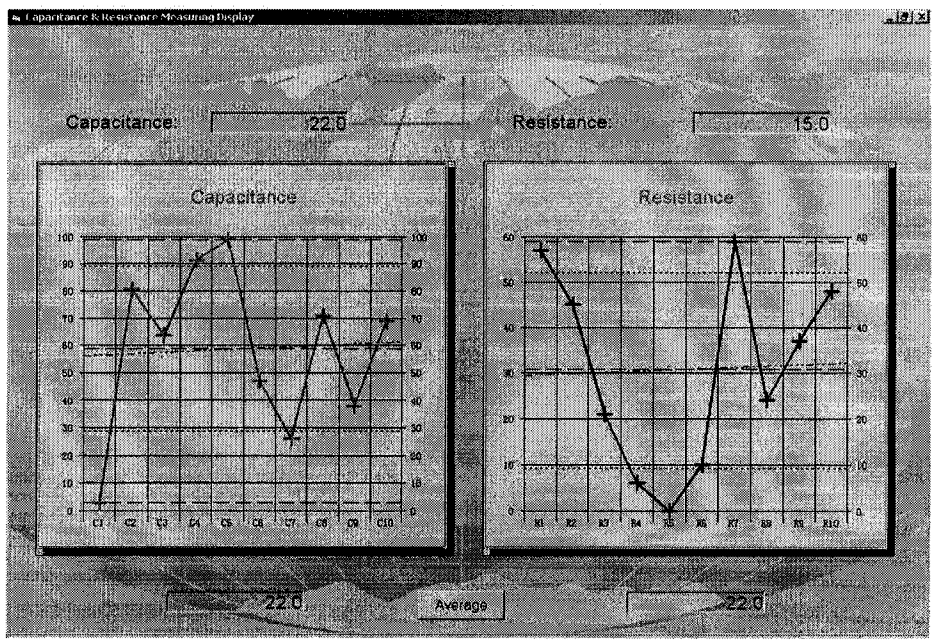

Figure 3-32: The interface picture of the management program.

```
   bSending = 1
Else
   varOut = "1R"    ' address 01 , resistance data
   bSending = 0
End If
// Sending a reply in the slave nodes
sprintf(cdataA, "%10.1f", tempd1/MEASURING_NUM);
for(i=0; i< SCI_DATA_LENGTH-1; i++)
{
      scidataA_C[i+1] = cdataA[i];      // Send data
}
/* If "C"-Capacitance data   */
scidataA_C[0]=67;
/* If "R"-Resistance data    */
scidataA_C[0]=82;
```

3.3.5 Results

As the simulations are conducted in Matlab, a 50KHz signal is employed in the experiments of the DSP-based impedance measuring system. Similar results are also obtained by this physical system. Figures (3-33a and 3-33b) show the linearity of the conductance and capacitance measurements in which the linear regression models are also given as

$$\frac{1}{\overline{y}[n]} = 0.0015578 \times \text{Resistance} + 4.20033 \times 10^{-6} \tag{3.18}$$

$$\overline{y}[n] = 21.786 \times \text{Capacitance} - 9.4273 \tag{3.19}$$

where

$\overline{y}[n]$ is the mean of the output y[n] of the digital PSD.

In Figure (3-33), the correlation coefficients between the measured data and the simulated data are greater than 0.999. In addition, the capacitance measurement can meet the resolution of 0.03pF. In other words, the DSP-based measuring system has good linearity and good resolution in the measurements. Therefore, it can be used to measure the conductance and capacitance in future research.

3.4 Concluding Remarks

This chapter outlines the design and implementation of a DSP-based impedance measuring instrument revised from a previous analog design. This system gives the platform to measure the component fractions of oil/gas/water. Next, the corresponding experiments will be discussed in Chapter 4.

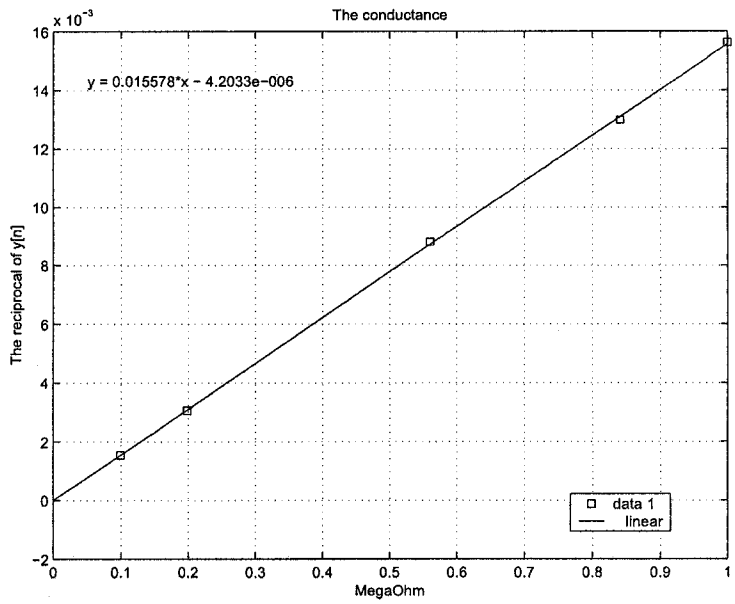

(a) Conductance

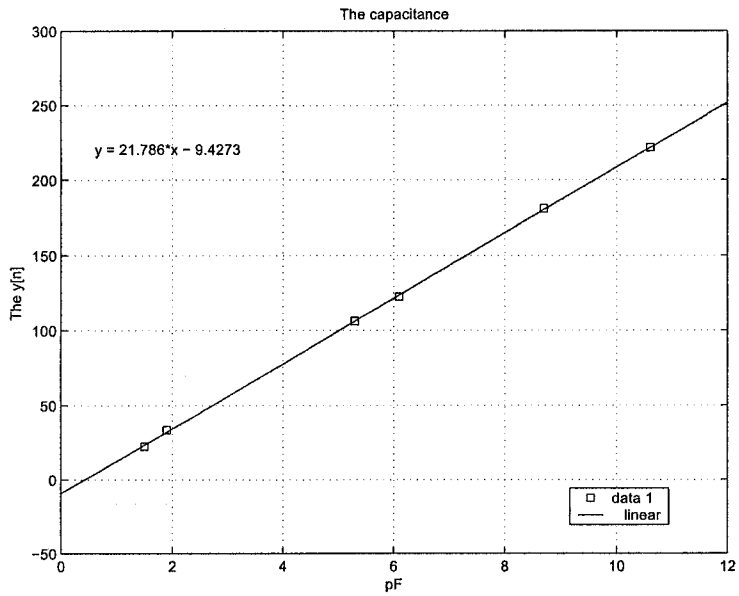

(b) Capacitance

Figure 3-33: The linearity of the DSP measuring system.

Chapter 4

Experimental Results

The DSP-based impedance measuring instrument has been designed and implemented to measure the conductance and capacitance across the impedance sensor in crude oil. This chapter will give a discussion on the experiments of using this impedance measuring instrument and the experimental results under different conditions. It will first discuss the design of experiments. Next, the result and analysis of each experiment are presented.

4.1 Design of Experiments

The final objective of this PPSC research project is to measure the component fractions in crude oil using an impedance-based multiphase flowmeter. A cyclone flow rotator is assumed to uniform an arbitrary flow into a stratified flow in terms of the different gravities of the gas/oil/water in crude oil. Therefore, the experiments in this research only focus on the stratified multiphase flows.

Figure (4-1) shows the devices used in the experiments, which include a manual valve and two glass-measuring cylinders. The manual valve is used to control the levels of two glass cylinders. The impedance sensor is installed in a measuring cylinder without a gradient, and the measuring cylinder with a gradient is employed to

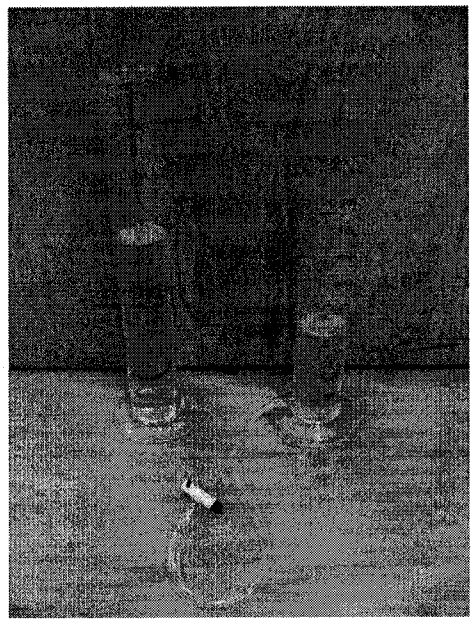

Figure 4-1: The picture of the glass measuring cylinders.

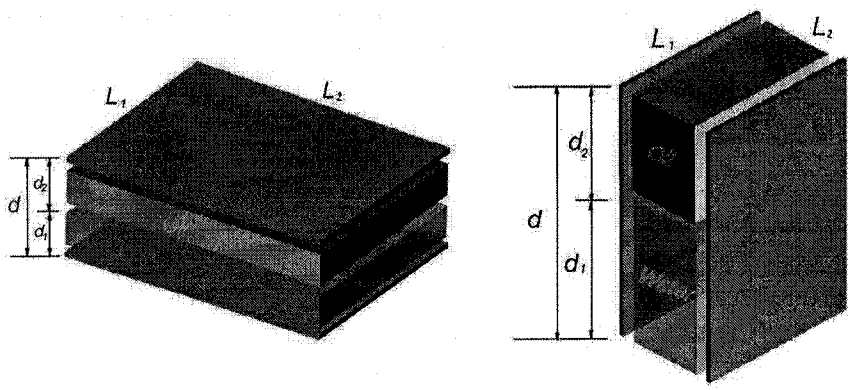

(a) Horizontal electrodes. (b) Vertical electrodes

Figure 4-2: The diagrams for horizontal electrodes and vertical electrodes.

control the mixture fractions in the impedance sensor. Parallel plates are chosen as the electrodes of the impedance sensor in the experiments, and two electrode configurations have been considered in Figures (4-2a and 4-2b): horizontal electrodes and vertical electrodes.

Horizontal electrodes

As portrayed in Figure (4-2a), two stratified dielectric materials, oil and water, are filled between two horizontal electrodes. The equivalent circuit of this horizontal measuring sensor is similar to two capacitors in series.

So

$$\frac{1}{C_{horizontal}} = \frac{1}{C_{water}} + \frac{1}{C_{oil}} \tag{4.1}$$

Substituting the formula (1.1), Equation (4.1) can be rewritten as

$$C_{horizontal} = \frac{\varepsilon_0 \varepsilon_{water} \varepsilon_{oil} L_1 L_2 / d}{\varepsilon_{water} - (\varepsilon_{water} - \varepsilon_{oil}) d_1 / d} \tag{4.2}$$

Vertical electrodes

Figure (4-2b) shows a vertical measuring sensor. In contrast to the horizontal sensor, its equivalent circuit is two capacitors in parallel.

So

$$C_{vertical} = C_{water} + C_{oil} \tag{4.3}$$

Again, substituting the formula (1.1), Equation (4.3) can be rewritten as

$$C_{vertical} = \frac{\varepsilon_0 L_1 d}{L_2} \left[\frac{d_1}{d} (\varepsilon_{water} - \varepsilon_{oil}) + \varepsilon_{oil} \right] \tag{4.4}$$

Based on Equation (4.2) and Equation (4.4), the capacitance changing curves can be drawn in Figure (4-3). In Figure (4-3a), the output capacitance is nearly the same when the water ratio is changing from 0% to 60% in stratified mixtures. This shows that the horizontal electrodes are not suitable for the measurements when the

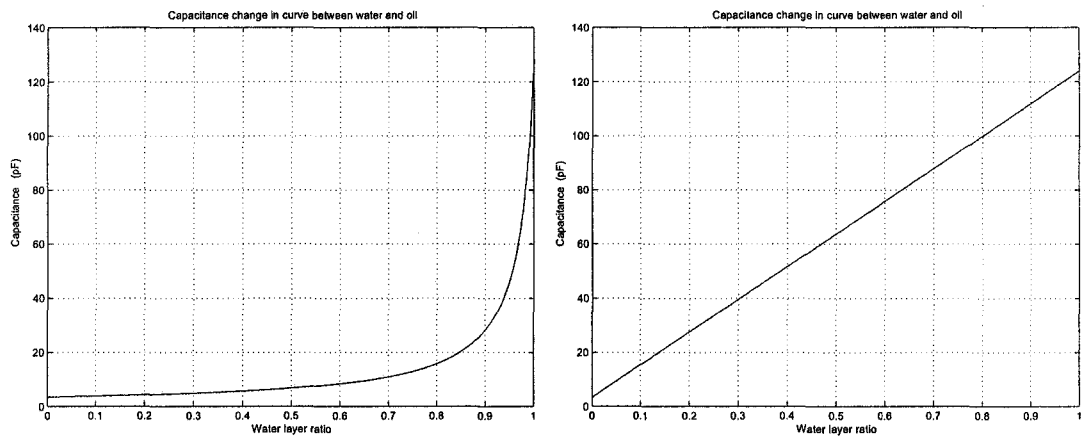

(a) Horizontal electrodes (b) Vertical electrodes

Figure 4-3: The capacitance changing curves for horizontal electrodes and vertical electrodes.

water ratio is less 60% in the mixtures. On the other hand, the output capacitance of vertical electrodes in Figure (4-3b) has good linearity with the water ratio in the mixtures. Therefore, the vertical electrodes are chosen in the experiments of this thesis.

Sensor shielding

Effect of a electrostatic shield in the experiments has been also tested. If no shield is placed outside the parallel plate electrodes, the electrodes will be not only an impedance sensor, but also an interference receiver. In Figure (4-4a), the sensing signal and the interference signals from the outside electromagnetic field both appear in the sensor output current. A grounded tin foil shield in Figure (4-5) is therefore used in the experiments to remove these interference signals from electrodes. A very smooth sine wave is obtained in Figure (4-4b), which shows that this tin foil shield does prevent electrodes from interference signals.

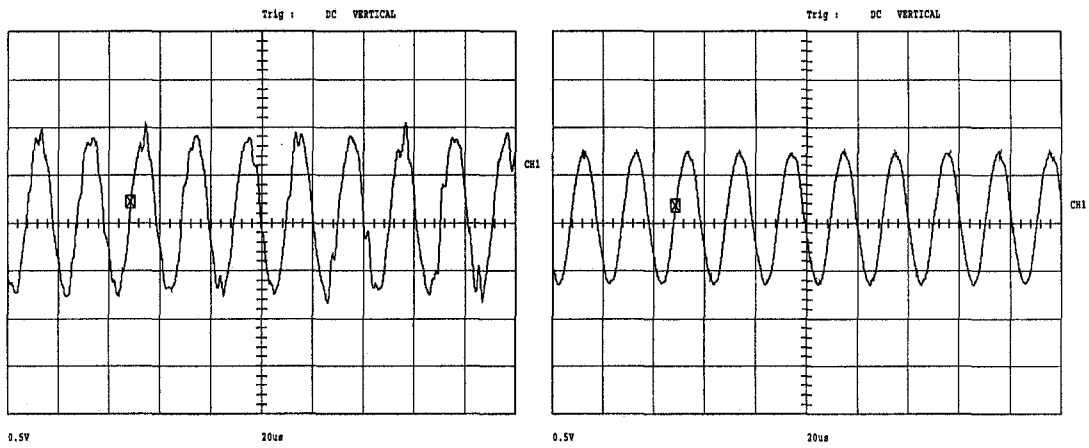

(a) Without a shield (b) With a shield

Figure 4-4: The performance with/without a shield outside the sensor.

Experimental scenarios

The experiments in this thesis are carried out on three different scenarios to verify whether this DSP-based impedance measuring instrument can be used to measure the component fractions in stratified mixtures. These experimental scenarios are

- air/water
- air/oil
- oil/water

For easy implementation, the air is employed in the experiments instead of the gas because their permittimities are nearly the same ($\varepsilon_r \approx 1.0$). In the experiments, the parameters in Figure (4-2b) are selected as below:

L_1=0.01, meters
L_2=0.04, meters
d=0.1, meters

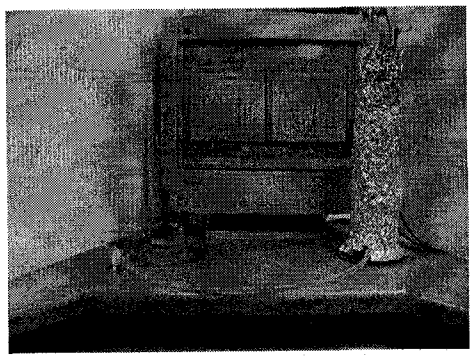

Figure 4-5: The shielded experimental measuring system.

ε_0=8.854 $\times$ 10^{-12}, Free space permittivity, frads/meters

ε_{air}=1.0, Air relative permittivity

ε_{oil}=2.2, Oil relative permittivity

ε_{water}=80, Pure water relative permittivity,

=78, Dyed water in Scenario Three

4.2 Scenario One: Air/Water

The experiments in scenario one are employed to measure capacitances and conductances between two vertical electrodes when water ratios are increased from 0 to 1 (0% $\sim$ 100%). By the limitation of the smallest gradient sign on the glass-measuring cylinder, the measurements are carried out on fifteen different water levels. With each water level, the data processing software can automatically store twenty measuring results and display their average values on the bottom of the screen.

Results analysis

According to the final measuring results listed in Table (4.1), the capacitance and conductance data are drawn in Figure (4-6a and 4-6b), in which fifteen water levels are normalized into water ratios from 0 to 1.

No.	Measured average capacitance (y[n])	Measured average conductance (y[n])	Theoretical capacitance (pF)
0	29.45687	8.26108	0.22135
1	294.97110	106.052000	1.47040
2	337.99300	78.013630	2.71944
3	368.48320	52.445780	3.96849
4	400.25400	20.220120	5.21754
5	409.10810	7.340903	6.46658
6	418.97480	8.316511	7.71563
7	426.84350	19.500100	8.96468
8	436.56900	28.996200	10.21372
9	454.61680	40.521390	11.46277
10	484.01200	49.197820	12.71181
11	514.79360	59.434700	13.96086
12	531.17880	67.917920	15.20991
13	543.61360	73.766300	16.45895
14	560.27770	78.749890	17.70800

Table 4.1: The final measuring results in Scenario One.

Capacitance In terms of the sensor capacitance data shown in Figure (4-6a), the basic fitting tools in Matlab give a linear regression model when the water ratio is greater than 0.07 (Water Ratio $>$ 0.07):

$$\text{Capacitance} = 260.55 \times (\text{Water Ratio}) + 301.97 \tag{4.5}$$

Further analysis shows that the correlation coefficients between the predicted data and the last fourteen measured data are greater than 0.9866. The measuring capacitances have good linearity when the water ratio is greater than 0.07 (Water Ratio $>$ 0.07). This linear result is in accordance with the theoretical analysis in Equation (4.4). However, the measured capacitances are not proportional to the water ratios when the water ratio is less than 0.07 (Water Ratio $<$ 0.07).

Conductance In order to prevent erosion from crude oil, the electrodes are normally coated with the insulated layers, so no DC current can be conducted from one elec-

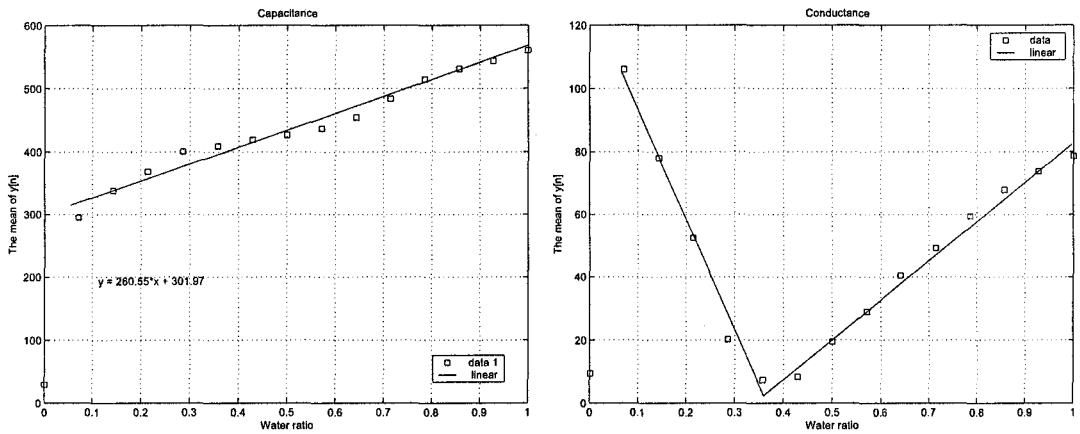

(a) Capacitance (b) Conductance

Figure 4-6: The diagrams for the final measuring results in Scenario One.

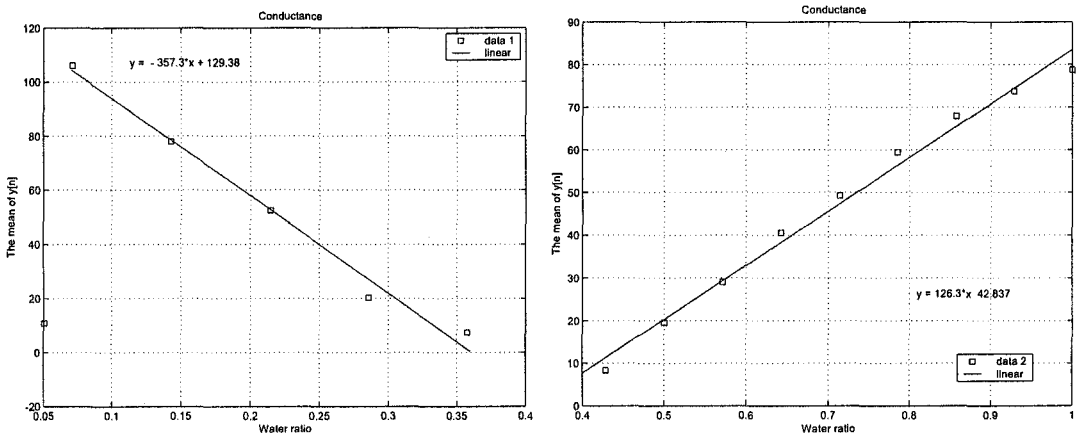

(a) Conductance in the low water ratios (b) Conductance in the high water ratios

Figure 4-7: The diagrams for the measuring conductances in Scenario One.

trode to another electrode, and the DC conductances between two electrodes are zero. However, if an AC signal is fed into the electrodes, the AC conductances, known as dielectric-loss conductances, can be detected in the experiments, which are shown in Figure (4-6b).

In theory, the AC conductances are basically the DC conductances modified by the shift effect. Usually, the AC conductances are less than the DC conductances. Due to the complex nature of the skin effect, no theoretical model is currently available to analyze the AC conductances; however, they can be obtained by experiments. Similar to the DC conductance components shown in Figure (2-13), they also have 90° phase difference with the capacitive reactance.

As discussed in capacitance measurements, the non-linear zone is located near the origin of the coordinates (Water Ratio < 0.07). The remaining part is divided into two linear zones. When the water ratio is greater than 0.07 and less than 0.4 ($0.07 <$ Water Ratio < 0.4), increasing water ratios will decrease the loss conductances. On the other hand, if the water ratio is greater than 0.4 (Water Ratio > 0.4), the loss conductances will be increased with water ratios. In terms of Figure (4-7a and 4-7b), the Matlab tools give the following linear regression models:

$$\text{Conductance} = -357.3 \times (\text{Water Ratio}) + 129.38 \tag{4.6}$$

where $\text{Water Ratio} \in (0.07, 0.4)$;

$$\text{Conductance} = 126.3 \times (\text{Water Ratio}) + 42.837 \tag{4.7}$$

where $\text{Water Ratio} \in (0.4, 1)$.

In the linear zones, the correlation coefficients between the measured data and the predicted data are greater than 0.9934. However, when the water ratio is less than 0.07 (Water Ratio < 0.07), the changing conductances do not follow these two

No.	Measured average capacitance (y[n])	Measured average conductance (y[n])	Theoretical capacitance (pF)
0	29.45687	8.26108	0.22135
1	29.65724	8.50200	0.24032
2	30.27036	8.75283	0.25930
3	31.82451	9.34911	0.27827
4	33.19509	9.98498	0.29724
5	34.44445	10.03300	0.31621
6	35.44643	10.53858	0.33519
7	36.66202	10.99655	0.35416
8	37.80292	11.50275	0.37313
9	38.93204	11.99748	0.39211
10	40.10469	12.44168	0.41108
11	40.81390	12.82504	0.43005
12	41.35981	13.05025	0.44902
13	41.98884	13.36034	0.46800
14	42.47823	13.69012	0.48697

Table 4.2: The final measuring results in Scenario Two.

linear regression models.

4.3 Scenario Two: Air/Oil

The experiments in scenario two are done to measure capacitances and conductances between two vertical electrodes when oil ratios are increased from 0 to 1 (0% $\sim$ 100%). As discussed in scenario one, the measurements are also carried out on fifteen different oil levels. In each oil level, the data processing software automatically stores twenty measuring results and displays their average values on the bottom of the screen.

Results analysis

In terms of the final measuring results listed in Table (4.2), the capacitance and conductance data are drawn in Figure (4-8a and 4-8b), in which fifteen oil levels are normalized into oil ratios from 0 to 1.

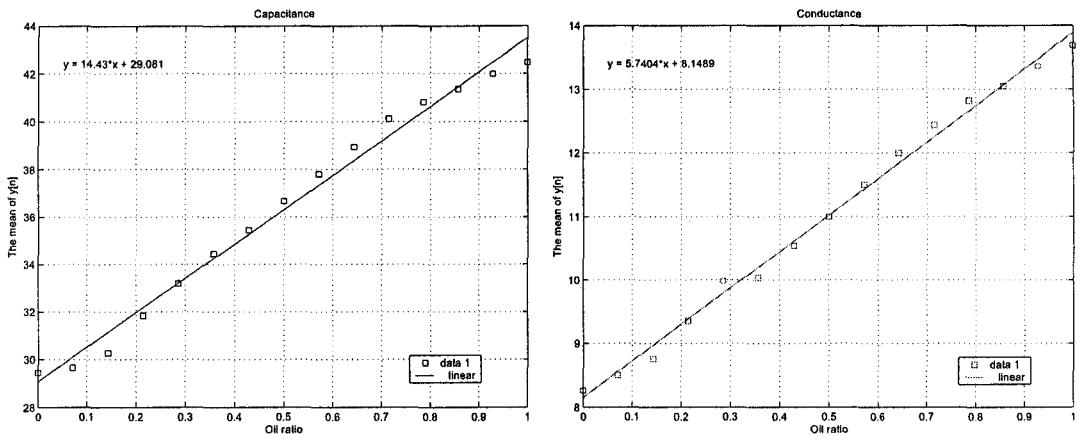

(a) Capacitance (b) Conductance

Figure 4-8: The diagrams for the final measuring results in Scenario Two.

Capacitance Based on the sensor capacitance data shown in Figure (4-8a), the basic fitting tools in Matlab give a linear regression model:

$$\text{Capacitance} = 14.43 \times (\text{Oil Ratio}) + 29.081 \tag{4.8}$$

Further analysis shows that the correlation coefficients between the measured data and the predicted data are greater than 0.9933. In other words, the measuring capacitances have good linearity, which is in accordance with the theoretical analysis in Equation (4.4).

Conductance Other than the loss conductances measured in scenario one, the measured loss conductances in scenario two have good linearity with the oil ratios; namely, the loss conductances are proportional to the oil ratios. According to the conductance data in Figure (4-8b), the Matlab tools give a linear regression model:

$$\text{Conductance} = 5.7404 \times (\text{Oil Ratio}) + 8.1489 \tag{4.9}$$

In Figure (4-8b), the correlation coefficients between the measured data and the

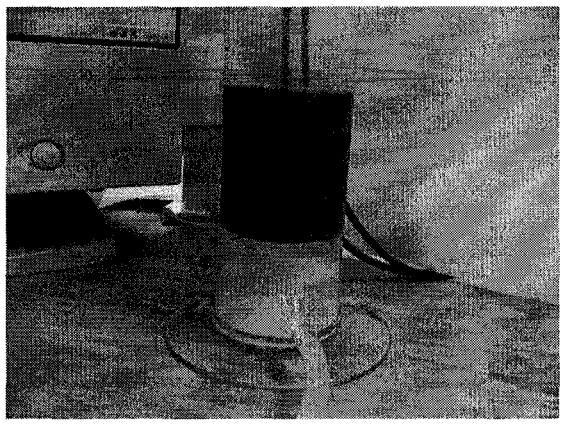

Figure 4-9: The stratified water and oil in Scenario Three.

predicted data are greater than 0.99699.

4.4 Scenario Three: Oil/Water

The experiments in scenario three are used to measure capacitances and conductances between two vertical electrodes when water ratios are increased from 0 to 1 and oil ratios are decreased from 1 to 0 (namely, Water Ratio + Oil Ratio = 1). In Figure (4-9), the tap water is dyed white in order to observe the changes in the water/oil levels. As the previous two experiments, the measurements are also carried out on fifteen different water/oil levels. In each water/oil level, the data processing software stores twenty measuring results and displays their average values on the bottom of the screen.

Results analysis

In terms of the final measuring results listed in Table (4.3), the capacitance and conductance data are drawn in Figure (4-10a and 4-10b), in which fifteen water/oil levels are normalized into water ratios from 0 to 1.

No.	Measured average capacitance (y[n])	Measured average conductance (y[n])	Theoretical capacitance (pF)
0	63.73018	9.55038	0.48697
1	173.96690	39.98667	1.68542
2	206.86970	32.02092	2.88387
3	227.66670	17.39402	4.08233
4	242.67260	4.19264	5.28078
5	255.91260	9.04884	6.47923
6	275.69390	23.92959	7.67768
7	304.25890	36.80481	8.87614
8	333.30850	43.95237	10.07459
9	349.02410	45.76104	11.27304
10	360.28310	48.54134	12.47149
11	383.33400	50.95983	13.66994
12	403.15080	55.95395	14.86840
13	423.45530	60.57764	16.06685
14	442.34970	64.38626	17.26530

Table 4.3: The final measuring results in Scenario Three.

Capacitance According to the sensor capacitance data shown in Figure (4-10a), the basic fitting tools in Matlab give a linear regression model when the water ratio is greater than 0.07 (Water Ratio $>$ 0.07):

$$\text{Capacitance} = 283.27 \times (\text{Water Ratio}) + 161.24 \tag{4.10}$$

Further analysis shows that the correlation coefficients between the predicted data and the measured data are greater than 0.998 (Water Ratio $>$ 0.07). In other words, the measuring capacitances have a good linearity when the water ratio is greater than 0.07, which is in accordance with the theoretical analysis in Equation (4.4).

Conductance As shown in Figure (4-10b), the changing pattern of the measured loss conductances in scenario three is a combination of patterns of conductances measured in scenario one and scenario two. When the water ratio is less than 0.07 (Water Ratio $<$ 0.07), no relationship can be obtained between the measured con-

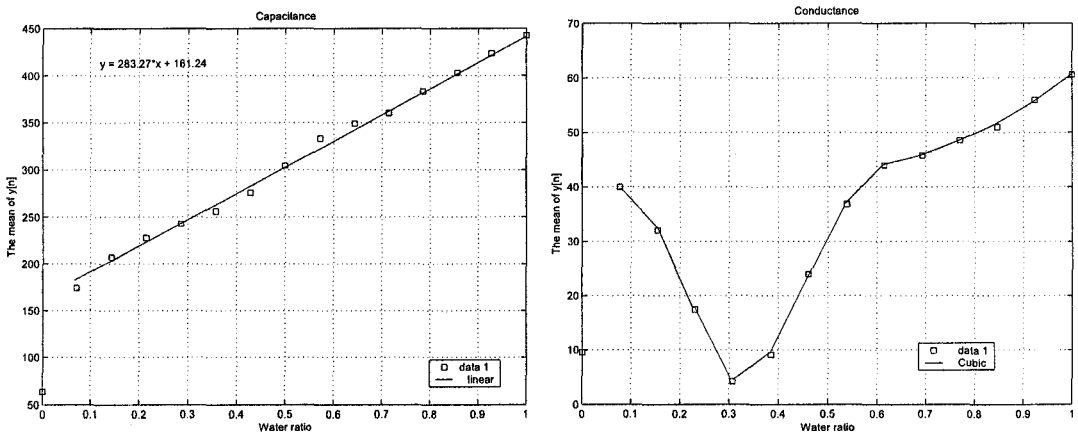

(a) Capacitance (b) Conductance

Figure 4-10: The diagrams for the final measuring results in Scenario Three.

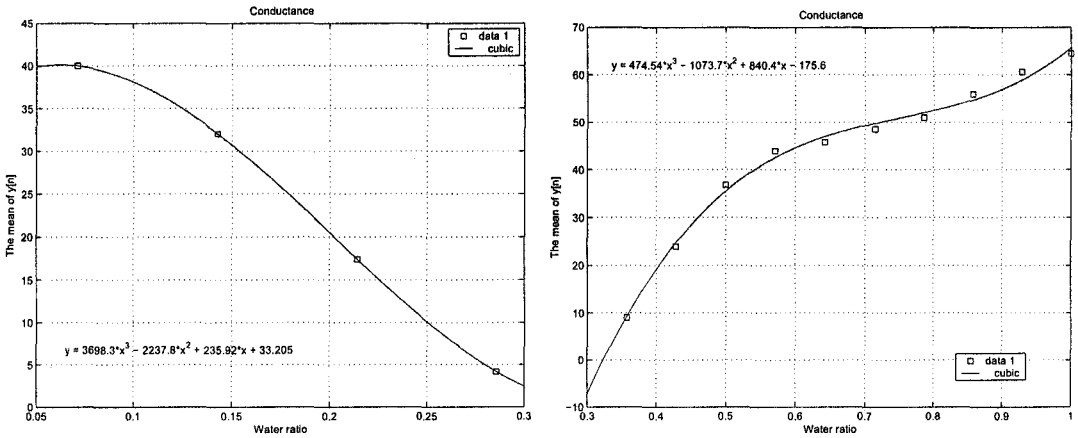

(a) Conductance in the low water ratios (b) Conductance in the high water ratios

Figure 4-11: The diagrams for the measuring conductances in Scenario Three.

ductances and the water ratios, which is the same as the experiments in scenario one. When the water ratio is greater than 0.07 (Water Ratio $>$ 0.07), two linear regression models are used in scenario one; however, they cannot be used in scenario three because of the effect of the oil in the experiments. Instead, two cubic regression models are obtained in scenario three. Moreover, in scenario three, the the zero loss conductance occurs when the water ratio is around 0.3, which is different from the zero loss conductance in scenario one.

Two cubic regression models for the loss conductances are:

$$\begin{aligned} \text{Conductance} &= 3698.3 \times (\text{Water Ratio})^3 - 2237.8 \times (\text{Water Ratio})^2 \\ &\quad +235.92 \times (\text{Water Ratio}) + 33.205 \\ &\quad \text{where} \quad \text{Water Ratio} \in (0.07, 0.3) \end{aligned} \tag{4.11}$$

$$\begin{aligned} \text{Conductance} &= 474.54 \times (\text{Water Ratio})^3 - 1073.7 \times (\text{Water Ratio})^2 \\ &\quad +840.4 \times (\text{Water Ratio}) - 175.6 \\ &\quad \text{where} \quad \text{Water Ratio} \in (0.3, 1.0) \end{aligned} \tag{4.12}$$

In Figure (4-10a and 4-10b), the correlation coefficients between the measured data and the predicted data are greater than 0.9972. In other words, the measured conductances match these two cubic models when the water ratio is greater than 0.07 (Water Ratio $>$ 0.07).

4.5 Summary of Experiments

In the previous three experiments, the water ratio is the most significant factor in the capacitance and conductance measurements of the air/oil/water mixtures. When the water ratio is between 0 and 0.07, the capacitances and loss conductance are changed dramatically, and no regression models can be obtained in the experiments. However, when the water ratio is greater than 0.07, the corresponding capacitance and conductance regression models can be accurately achieved in the experiments. As a result, the impedance measurements should be used to measure component fractions in the region (Water Ratio $>$ 0.07).

Analysis across the three experiments shows that the capacitances and loss conductances measured in scenario one are higher than the results obtained in scenario three when their water ratios are the same. The regular tap water is employed in scenario one, whereas the dyed water is used in scenario three. Therefore, the measured impedances are not only dependent on the water ratio in the experiments, but also on the purity of the water. This is a very important observation for future research in subsea crude oil because the same issue will occur in sea water that is not uniformly saline in different oceans, and has a specific conductance of approximately 50,000 $\mu S/cm$.

4.6 Concluding Remarks

This chapter discusses the design of experiments and the three different mixutre experiments that were performed to determine the relationships among the individual components. The measured capacitances in the three experiments are all in accordance with the theoretical analysis in Equation (4.4), which means that the DSP-based impedance measuring instrument can be employed to measure the component fractions in the air/oil/water mixture. The next chapter will give the conclusion and future work that can performed within this area of research.

Chapter 5

Conclusion and Future Work

The research presented in this thesis is focused on the design and implementation of a DSP-based impedance measuring instrument that is developed for the subsea multiphase measurement in particular. This chapter will first give the conclusion for the research described in this thesis. Next, suggestions for future work will be discussed.

5.1 Conclusion

A DSP-based impedance measuring instrument has been successfully implemented to measure capacitances and conductances from the multiphase flow of crude oil. Experimental results show that this measuring device has both good linearity and good resolution in the capacitance and conductance measurements.

In Chapter 3, "Design and Implementation of an impedance-based measuring instrument", an analog solution is tested at the beginning of the research, in which the principle and implementation of the stray-immune current detector, the DDS-based 90° phase shifter and the analog PSDs are described in detail. The testing results show that the measuring accuracy of this analog instrument cannot meet the requirement of the research due to the noise and poor stability in the measurement.

A digital signal processing concept has then been introduced in the research. This technique reduces significantly the need for the analog circuit, and implements the 90° phase shifter and PSDs in the digital domain. Simulations in Matlab show that this DSP method has both good linearity and good resolution in the capacitance and conductance measurements. As a result, a realtime digital solution has been designed by using a DSP chip, TMS320F2812 from Texas Instruments, to perform data acquisition and signal analysis simultaneously. In addition to this DSP measuring system, a supervisory computer is used to analyze and display the measuring data from the DSP system. In summary, this DSP-based impedance measuring instrument is composed of the following three parts:

- Signal conditioning part - including the stray-immune current detector, the AC instrumentation amplifier, the voltage level shifter, the serial communication voltage converter and the power supply.
- Digital signal processing part - including the eZdsp^{TM} F2812 development board and the C language processing software.
- Supervisory part - including the supervisory computer and the VB data management software.

The calibrating tests of this DSP-based impedance measuring instrument show less than 0.1% errors between the input impedances and the measured impedances. In addition, the stray-immune tests show that the measured capacitances have a low dispersion when different length cables are used between the impedance sensor and the measuring instrument. This result confirms that this measuring device has an instinctive stray-immune characteristic, which is essential to the impedance sensor subsea installation in the research.

In Chapter 4, "Experimental Results", the experiments in three different scenarios are carried out to verify the relevance of this instrument for the measurements in multiphase flows. First, the vertical parallel electrodes are compared to the horizontal electrodes. The former configuration gives a linear output with a high sensitivity and has been therefore selected in the experiments. Next, the tests have been performed in three different scenarios (air/water, air/oil, and oil/water). In each scenario, the mathematical regression models are given to the capacitance and conductance measurements. The error analysis shows less than 1.5% measuring error between the measured impedances and the predicted impedances from the regression models. In other words, a maximum 1.5% measuring error occurs in the component fraction measurements, which is better than the current industrial requirement $\pm 5\%$ [10].

The water fraction has been also found to play a dominant role in the capacitance and conductance measurements of the air/oil/water mixtures. When the water fraction is less than 0.07, no regression models can be acquired from the experiments, which is the reason why the impedance-based multiphase flowmeter requires a continuous water flow in the measurements. In addition to the water fraction, the water purity is another important factor in the mixture measurements. Tests show that the purer water has the higher impedance output at a certain water fraction.

5.2 Future Work

The DSP-based impedance measuring instrument described in this thesis is a success and has had the characteristics for the use in the offshore oil & gas industry; however, several suggestions for future work can be added. For instance, an onboard sine wave signal generator and a higher performance digital signal processor will be selected for further improvement of this instrument. Reference impedances and self-calibration will also be considered in the future research to provide a complete industrial solution for an impedance-based multiphase flowmeter.

(1) Onboard sine wave signal generator A function generator (HP 3310A) is employed to generate the 50KHz sine wave for the measuring system in this thesis. However, the compact design of the measuring system requires an onboard sine wave signal generator to replace this HP function generator. According to the sine wave generation techniques described in the application notes from National Semiconductor [29], the Wein bridge method is selected for the future design of the onboard sine wave signal generator because the method used has extremely low distortion (0.01%).

(2) A higher performance digital signal processor In this research, TMS320F2812 is selected as the digital signal processor, which operates at 150MHz (6.67ns Cycle Time) and supports 12-Bit, 500Ksps dual-channel ADC simultaneous sampling. The performance of this DSP chip is sufficient to the current research. However, this processor has two significant drawbacks.

- A fixed-point digital signal processor.
- A limited memory for the user's programme and data.

Since this processor does not support the floating-point multiplication, in order to obtain the high accuracy in the multiplications, the long integer type variables should be assigned as big as possible, so that the overflow sometimes occurs in the calculations.

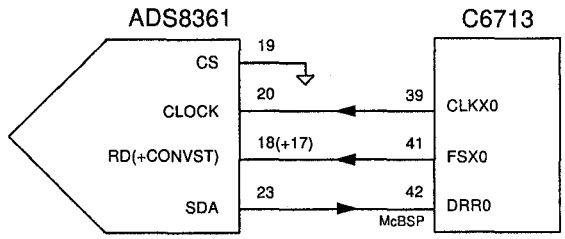

Figure 5-1: The communication interface between ADS8361 and TMS320C6713 [31].

In addition, this processor does not have enough user's free memory spaces that can be used in the FFT operations. As mentioned in Chapter 3, only 18K-Word program and data memory can be used in the programming due to the huge system reservation in the total addressable 4M-Word memory spaces. Therefore, the signal processing program in this thesis has to choose 256-point FFT in the signal processing, which also reduces the accuracy of the FFT operations.

In this way, TMS320C6713, a higher performance floating-point digital signal processor, is brought forward to future research. This processor operates at 225MHz, has 8K-Byte L1 memory, 256K-Byte L2 memory and 512M-Byte total addressable external memory spaces [30]. However, its ADC unit cannot perform 500K samples per second like TMS320F2812. Instead, an external ADC chip (ADS8361) or its evaluation module (ADS8361EVM), is employed in the new system, which can perform 16-Bit, 500kSPS, dual channel simultaneous sampling. As shown in Figure (5-1), the sampled data can be directly transmitted to multi-channel buffered serial ports (McBSPs) of TMS320C6713 via high-speed serial communication [31].

(3) Reference impedances Reference impedances are used to reduce the measuring drifts caused by the temperature and power supply changes. In Chapter 2, a thermal coupling method is used to construct an impedance reference system; however, it is difficult and expensive to be implemented in real applications. Therefore, a relatively simple solution should be investigated in the future research.

(4) Self-calibration This characteristic is a necessary requirement for the offshore multiphase flowmeters. Due to the harsh environment at sea, these flowmeters cannot be calibrated easily and frequently. Therefore, the future impedance measuring instrument should include several low temperature coefficient precise capacitors and resistors in the circuit. By these reference elements, the self-calibrating process can be performed everyday or as needed.

5.3 Concluding Remarks

This thesis first discusses the background of the impedance measuring techniques and the principles of the impedance signal detection and demodulation. It then illustrates the design and implementation of a DSP-based impedance measuring instrument. Next, the calibration tests and the mixture component fraction measurements are performed in the thesis. The results show this DSP-based impedance measuring instrument can be employed in the component fraction measurements of the air/oil/water mixtures. This chapter then discusses the conclusion for the thesis and future work that could be performed in this area of research.

Appendix A

Design Diagrams

A.1 The schematic diagram of the DSP signal conditioning board

A.2 The PCB diagrams of the DSP signal conditioning board

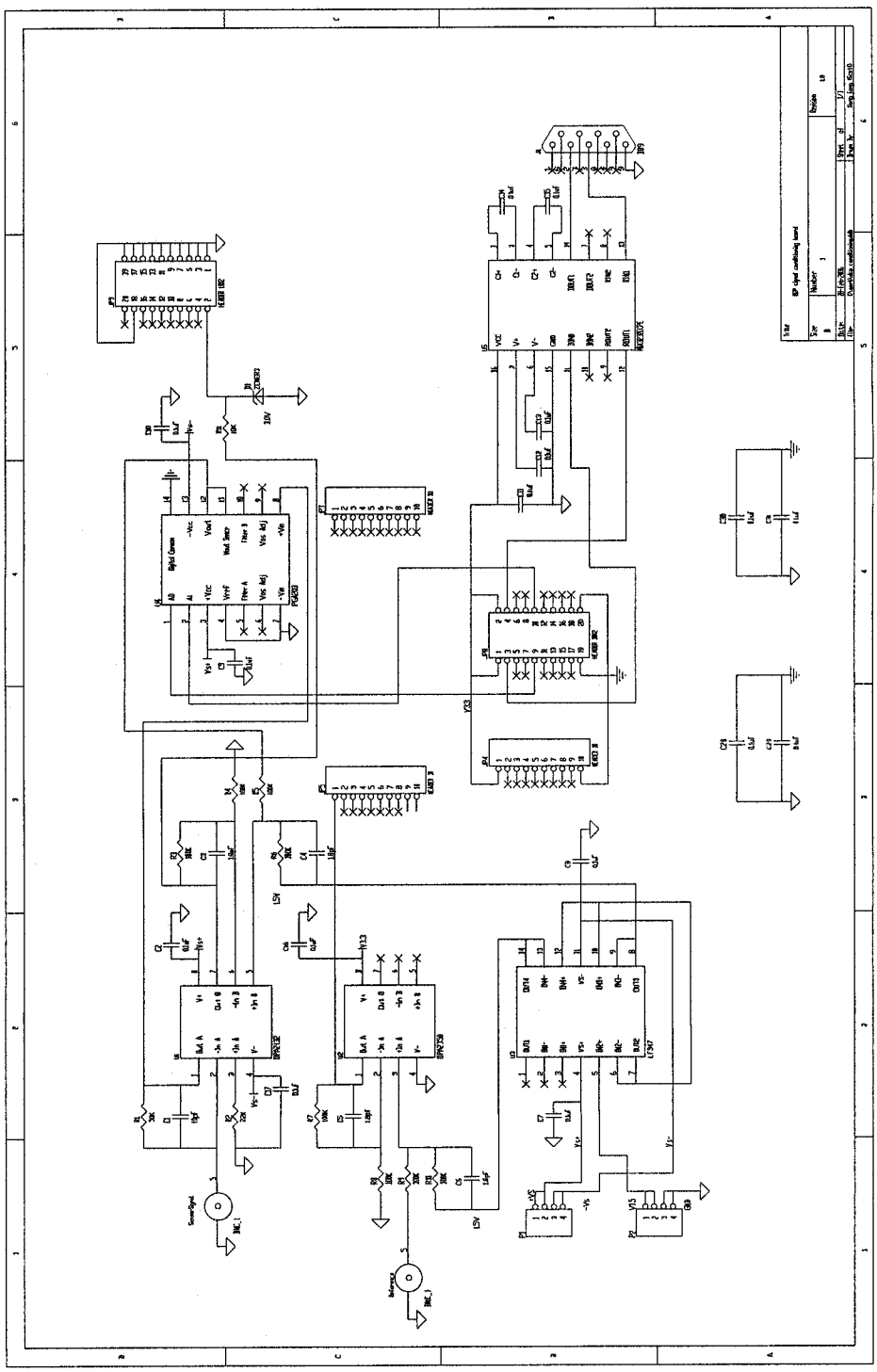

Figure A.1: DSP signal conditioning board schematic diagram.

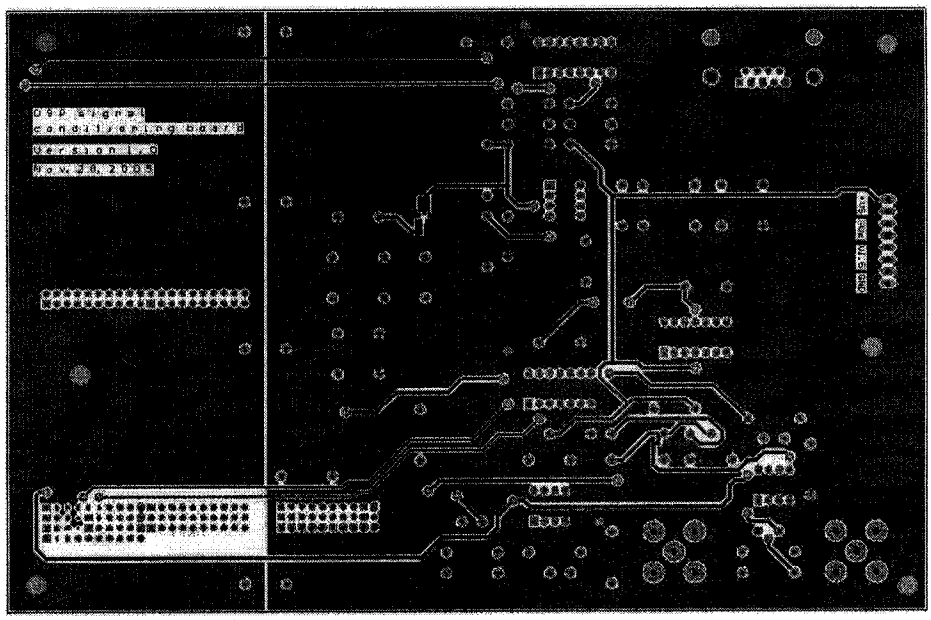

(a) Top side

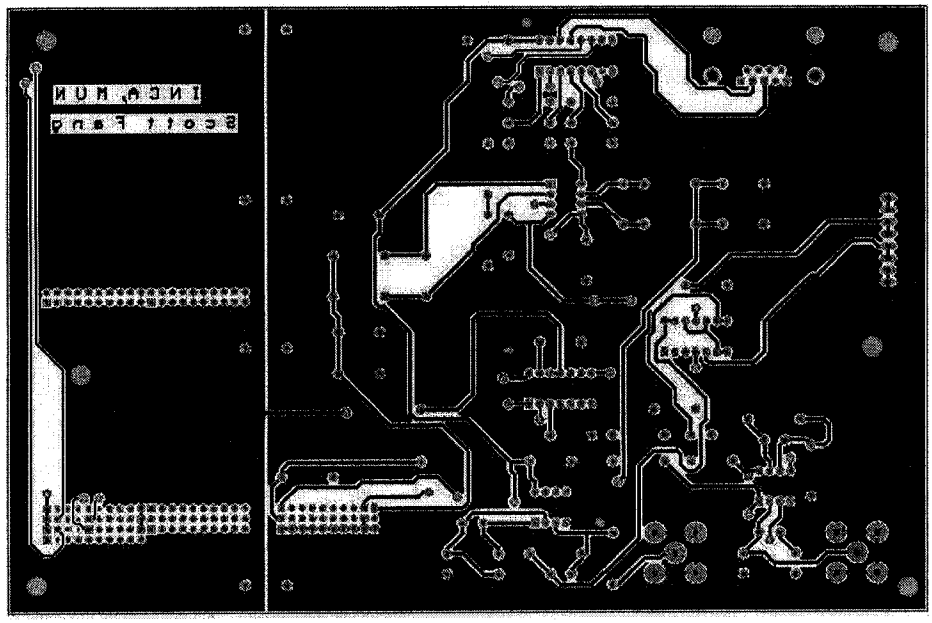

(b) Bottom side

Figure A.2: The PCB diagrams of the DSP signal conditioning board.

Appendix B

Source Code Listings

B.1 Simulation programs in Matlab

```
%%
%% Original filter program from
%%             Engr 8821/9821 - Winter 2005
%%             Module 5 - 9821 - Application
%%             FIR Filter Design for Signal in Noise
%% Rewrote by Xiang Fang (Scott), on Sep 30, 2005
%%

%%%% PART ONE: Setting up the Signals
clear all
close all
format long e
%%  Initial setup
num_fft_samples = 4096;
n = 1:1:num_fft_samples;
psd_type=1;   % 1 for in-phase (0 degree)
```

```
% psd_type=2;   % 2 for quadrature  (90 degree)
analysis_type=1;  %% 1 for Resistance
% analysis_type=2;   %  2 for Capacitance
if analysis_type==1
    Replications=10; % the number of different resistances
    y_out=zeros(Replications,1);
    x_out=[0.0987,0.1985,0.501,0.841,1.002,
              1.772,2.201,3.285,3.90,4.01];
elseif analysis_type==2
    Replications=7 %  the number of different capacitances
    y_out=zeros(Replications,1);
    x_out=[1.2,1.5,1.9, 5.3, 6.1, 8.7, 10.6];
end

for replica_n=1:9
for freq_n=1:1 % only 50KHz is selected
for experiment_n=1:Replications

if (experiment_n<10)
    filename1 = ['0', num2str(experiment_n)];
else
    filename1 = num2str(experiment_n);
end
filename3 = num2str(replica_n-1);
if analysis_type==1
   file = ['r0', filename1,'.00',filename3];
elseif analysis_type==2
   file = ['c0', filename1,'.00',filename3];
```

```
end %if analysis_type==1

%   Read data from Oscilloscope data files
[ch1_sample,ch2_sample,ch1mult,ch2mult,sec_per_div]
                  = filedata(file);
ch1temp = ch1mult .* ch1_sample;   % for signal input
ch1 = ch1temp - mean(ch1temp);
ch2temp = ch2mult .* ch2_sample;   % for reference input
ch2 = ch2temp - mean(ch2temp);

%  Apply Multiplier Function to signal and reference
if      psd_type==1
   x= ch1 .* ch2;
elseif psd_type==2
   % Form (pi/2) shifted reference signal
   % From time domain to frequency domain,
   % then back to time domain
   CH2 = fft(ch2,num_fft_samples);
   % Here FFT() is employed, so the omega range  is (0, 2*pi).
   % DTFT() function's range is (-pi, pi)
   CH2_NEW= CH2 .* j;  %%  shift pi/2 exp(j*pi/2);
   %(cos(w0*n+pi/2))->(j*pi*delta(w-w0)-j*pi*delta(w+w0))
   for I = (num_fft_samples/2+1):num_fft_samples,
      % points (1,2048) means the w from (0,pi)      ^
      % points (2049,4096) means the w from (pi,2*pi) or (-pi,0)
      CH2_NEW(I) = - CH2_NEW(I);
   end
   ch2_quadrature=ifft(CH2_NEW,num_fft_samples); % Inverse FFT
```

```
   x= ch1 .* ch2_quadrature;
end % (if psd_type==1)

[CH1,W] = dtft(ch1,num_fft_samples);
if psd_type==1
        [CH2,W] = dtft(ch2,num_fft_samples);
else
        [CH2,W] = dtft(ch2_quadrature,num_fft_samples);
end
%% X is freq. response for the output of the multiplier
[X,W] = dtft(x,num_fft_samples);
%%%% PART TWO : FILTER DESIGN
%% Design parameters - in two sets, for different design modes

mode = 1; %% mode = 1 to filter out AC signals
fprintf('\n ----------Mode= %d  --------------',mode)
if (mode == 1) %% To filter out AC
        delta1 = 0.02;
        delta2 = 0.01;
        delta = min(delta1, delta2);
        omega_p = 0.002*pi;
        omega_s = 0.01*pi;
        delta_omega = omega_s-omega_p;
        omega_c = omega_p + delta_omega/2;
end
%% Now design a Kaiser windowed FIR filter to these specifications
%% Kaiser window calculations
A=-20*log10(delta)
```

```
beta = 0.0;
if (A>50)
   beta = 0.1102 *(A-8.7);
elseif ((A >= 21) & (A <=50))
   beta = 0.5842*(A-21)^0.4 + 0.07886*(A-21);
end
M = (A-8)/(2.285*delta_omega);
M = ceil (M)
win = kaiser(M+1,beta);
alpha = M/2;
nh=0:1:M;
%% the ideal desired impluse response
if (mode == 1 )
   ir = (omega_c/pi)*sinc((omega_c/pi)*(nh-alpha));
   %% Using Matlab function sinc(x) = sin(pi*x)/(pi*x)
elseif (mode == 2)
   ir1 = (omega_c2/pi)*sinc((omega_c2/pi)*(nh-alpha));
   ir2 = (omega_c1/pi)*sinc((omega_c1/pi)*(nh-alpha));
   ir = ir1 - ir2 ;
end
ir_win = transpose(ir) .* win;
%% Transform into frequency
N = num_fft_samples;
[H,w]=dtft(ir_win,N);
delta1=(1+delta)*ones(N,1);
delta2=(1-delta)*ones(N,1);
delta3=delta*ones(N,1);
%%% PART THREE:
```

```
%%% Using the design to filter AC signals out of x_w
h = ir_win;
a = [1];
y = filter(h,a,x);  % in freq. domain: Y(w) = X(w) * H(w)
[Y,W] = dtft(y,num_fft_samples);
if replica_n==1
    y_out1(experiment_n,freq_n)=abs(mean(y))
elseif replica_n==2
    y_out2(experiment_n,freq_n)=abs(mean(y))
elseif replica_n==3
    y_out3(experiment_n,freq_n)=abs(mean(y))
elseif replica_n==4
    y_out4(experiment_n,freq_n)=abs(mean(y))
elseif replica_n==5
    y_out5(experiment_n,freq_n)=abs(mean(y))
elseif replica_n==6
    y_out6(experiment_n,freq_n)=abs(mean(y))
elseif replica_n==7
    y_out7(experiment_n,freq_n)=abs(mean(y))
elseif replica_n==8
    y_out8(experiment_n,freq_n)=abs(mean(y))
elseif replica_n==9
    y_out9(experiment_n,freq_n)=abs(mean(y))
end
end %for experiment_n=1:5
end %for freq_n
end % for replica_n
y_out= (y_out1 + y_out2 + y_out3 + y_out4 + y_out5
```

```
+ y_out6 + y_out7 + y_out8 + y_out9 ) ./ 9
figure
if analysis_type==1
    plot(x_out, abs(1 ./ y_out),'ks');grid;
elseif analysis_type==2
     plot(x_out, abs(y_out),'ks');grid;
end
%%%%%%%%%%%%%%%%%%%%%%%%%%%%%%%%%%%%%%%%%%%%%%%%%%%%%%%%%%%%%%%%%%%%%%%
%% No More
%%%%%%%%%%%%%%%%%%%%%%%%%%%%%%%%%%%%%%%%%%%%%%%%%%%%%%%%%%%%%%%%%%%%%%%
```

```
%% Original file reading program ( filedata.m ) from
%%            Dr. Masek and Andrew Oldford
%% Rewrote by Xiang Fang (Scott), on Sep 28, 2005
%%

function [ch1_sample,ch2_sample,ch1mult,ch2mult,sec_per_div]
                                    = filedata(filename)
fid = fopen(filename,'r');
A = fread(fid);
status=fclose(fid);
i = 1;
str = char(A(i:(i+5)))';
done = 0;
while(done == 0)
    if(str == 'XINCR ')
        done = 1;
    else
        i = i + 1;
        str = char(A(i:(i+5)))';
    end
end
i = i+6;
j = i;
while(char(A(j+1)) ~= ';')
    j = j+1;
end
sec_per_div_str = char(A(i:j))';
```

```
sec_per_div = str2double(sec_per_div_str);
i = j;
str = char(A(i:(i+5)))';
done = 0;
while(done == 0)
    if(str == 'YMULT ')
        done = 1;
    else
        i = i + 1;
        str = char(A(i:(i+5)))';
    end
end
i = i+6;
j = i;
while(char(A(j+1)) ~= ';')
    j = j+1;
end
temp_i=i;
ch1mult_str = char(A(i:j))';
ch1mult = str2double(ch1mult_str);
i = j;
str = char(A(i:(i+5)))';
done = 0;
while(done == 0)
    if(str == 'YMULT ')
        done = 1;
    else
        i = i + 1;
```

```
        str = char(A(i:(i+5)))';
    end
end
i = i+6;
j = i;
while(char(A(j+1)) ~= ';')
    j = j+1;
end
ch2mult_str = char(A(i:j))';
ch2mult = str2double(ch2mult_str);
i=temp_i; %% return to the first data place
str = char(A(i:(i+4)))';
done = 0;
while(done == 0)
    if(str == '44096')
        done = 1;
    else
        i = i + 1;
        str = char(A(i:(i+4)))';
    end
end
i = i+5;
ch1_sample = A(i:(i+4095));
str = char(A(i:(i+4)))';
done = 0;
while(done == 0)
    if(str == '44096')
        done = 1;
```

```
    else
        i = i + 1;
        str = char(A(i:(i+4)))';
    end
end
i = i+5;
ch2_sample = A(i:(i+4095));
%%%%%%%%%%%%%%%%%%%%%%%%%%%%%%%%%%%%%%%%%%%%%%%%%%%%%%%%%%%%%%%%%%%%%%%
%% No More
%%%%%%%%%%%%%%%%%%%%%%%%%%%%%%%%%%%%%%%%%%%%%%%%%%%%%%%%%%%%%%%%%%%%%%%
```

B.2 C programs in TMS320F2812

Please see files in the attached CD.

B.3 VB programs in the supervisory computer

Please see files in the attached CD.

Bibliography

[1] "Precise impedance measurement of electrical components," Jan. 2006. [Online]. Available: http://www.chenyang-ism.com/Impedance.htm

[2] E. Dykesteen, A. Hallanger, E. Hammer, E. Samnoy, and R. Thorn, "Non-intrusive three-component ratio measurement using an impedance sensor," *Journal of Physics E: Scientific Instruments*, vol. 18, no. 5, pp. 540–544, June 1985.

[3] S. M. Huang, A. L. Stott, R. G. Green, and M. S. Beck, "Electronic transducers for industrial measurement of low value capacitances," *J. Phys. E: Sci. Instrum.*, vol. 21, no. 3, pp. 242–250, Mar. 1988.

[4] S. Corneliussen, J. P. Couput, E. Dahl, E. Dykesteen, K. E. Frøysa, E. Malde, H. Moestue, P. O. Moksnes, L. Scheers, and H. Tunheim, "Handbook of multiphase flow metering," Mar. 2005. [Online]. Available: http://www.nfogm.no/docup/dokumentfiler/MPFM_Handbook_Revision2_2005_(ISBN-82-91341-89-3).pdf

[5] "conductance," Feb. 2006. [Online]. Available: http://physics.about.com/od/physicsglossaryc/g/conductance.htm

[6] L. K.Baxter, *Capacitive sensors : design and applications.* New York : IEEE Press, 1997.

[7] T. Bol and L. Scheers, "Multiphase flow metering per well, can it be justified?" July 2005. [Online]. Available: http://www.flowshow.nl/presentaties/MPFM, %20Ton%20Bol.pdf

[8] "Framo multiphase flow meters phasewatcher vx," Jan. 2006. [Online]. Available: http://www.framoeng.no/Files/Bulletins/FramoMultiphaseFlowMeters2003.pdf

[9] R. Thorn, G. A. Johansen, and E. A. Hammer, "Recent developments in three-phase flow measurement," *Meas. Sci Technol.*, vol. 8, no. 7, pp. 691–701, 1997.

[10] T. S. Whitaker, "Multiphase flow measurement: current and future developments [for offshore industry use]," in *Advances in Sensors for Fluid Flow Measurement, IEE Colloquium on*, Apr. 18, 1996, pp. 101–111.

[11] *TMS320F2810, TMS320F2811, TMS320F2812,TMS320C2810, TMS320C2811, TMS320C2812 Digital Signal Processors, Data Manual*, Texas Instruments, Dec. 2004, literature number: SPRS174L.

[12] "Agar mpfm-400 series multiphase flow meter," Jan. 2006. [Online]. Available: http://www.baggi.com/redazionali/MPFM400.pdf

[13] "Successful operational experience since december 1995 for 3 framo multiphase meters on bhp's hamilton, north hamilton, and lennox satellite platforms in liverpool bay," July 2004. [Online]. Available: http://www.framoeng.no/Files/Bulletins/LiverpoolBayaug.98.pdf

[14] "Multiphase flow meter mpfm 1900vi datasheet," Jan. 2006. [Online]. Available: http://www.roxar.com/files/Multiphase_Datasheet_-1-_1.pdf

[15] "White rose (oil field)," Apr. 2006. [Online]. Available: http://en.wikipedia.org/wiki/White_Rose_(oil_field)

[16] "Resonance in rlc circuits," Jan. 2006. [Online]. Available: http://zone.ni.com/devzone/conceptd.nsf/2d17d611efb58b22862567a9006ffe76/d32cfaf77aaa51c48625704b0056c841/$FILE/Lab7.pdf

[17] B. Hague and T. Foord, *Alternating Current Bridge Methods*, 6th ed. London : Pitman Press.

[18] D. Marioli, E. Sardini, and A. Taroni, "Measurement of small capacitance variations," in *Precision Electromagnetic Measurements, 1990. CPEM '90 Digest., Conference on*, June 11–14, 1990, pp. 22–23.

[19] M. L. Meade, *Lock-in amplifiers : principles and applications.* London : Peter Peregrinus Ltd on behalf of the Institution of Electrical Engineers, 1983.

[20] W. Q. Yang, A. L. Stott, and M. S. Beck, "High frequency and high resolution capacitance measuring circuit for process tomography," *Circuits, Devices and Systems, IEE Proceedings*, vol. 141, no. 3, pp. 215–219, June 1994.

[21] W. Q. Yang, S. K. Strandos, A. L. Stott, M. S. Beck, and J. A. Johansen, "A high frequency digital signal generator for capacitance tomographic imaging systems - requirements and realisation," *Proc. European concerted action on process tomography*, pp. 182–193, Mar. 24–26, 1994.

[22] W. Q. Yang and A. L. Stott, "A low-cost wide-frequency-range three-phase sine-wave signal generator using direct digital synthesis technique," *Meas. Sci. Technol.*, vol. 5, no. 7, pp. 866–868, July 1994.

[23] "Fpaa overview," Sept. 2005. [Online]. Available: http://www.anadigm.com/Sol_05.asp

[24] *eZdsp^{TM} F2812 Technical Reference*, Spectrum Digital, Inc., Sept. 2003, 506265-0001 Rev. F.

[25] *Anadigmvortex development board user manual*, Anadigm, Aug. 2003, uM030900-U010e.

[26] *TMS320x281x DSP Analog-to-Digital Converter (ADC) Reference Guide*, Texas Instruments, July 2005, literature number: SPRU060D.

[27] *TMS320x281x DSP System Control and Interrupts Reference Guide*, Texas Instruments, Mar. 2005, literature number: SPRU078C.

[28] "how to do ifft using only fft?" Nov. 2005. [Online]. Available: http://www.dsprelated.com/showmessage/25408/1.php

[29] *Sine Wave Generation Techniques*, National Semiconductor, Mar. 1981, application Note 263. [Online]. Available: http://www.web-ee.com/primers/files/AN-263.pdf

[30] *TMS320C6713 Floating-point Digital Signal Processors, Data Manual*, Texas Instruments, Nov. 2005, literature number: SPRS186L.

[31] *Interfacing the ADS8361 to the TMS320C6711 DSP*, Texas Instruments, Feb. 2003, literature number: SLAA164.